JOHNS HOPKINS UNIVERSITY **Applied Physics Laboratory**
Laurel MD 20723-6099

Memo No.
Charge No.
Date

To: John (Jay) Falker, PhD, Early Stage Portfolio Executive, Space Technology, NASA HQ, jfalker@nasa.gov, 202-358-4545

From: T. Miller[1], S. Kleinfelder[2], S. Barwick[2], D. Besson[3], Valery Chechin[6] , A. Connolly[4], German Gusev[6], T. Jaeger[1], G.W. Patterson[1], D. Rodgers[1], A. Romero-Wolf[5], Vladimir Ryabov[6], R. Schaefer[1], and H.B. Sequeira[1]

1 Johns Hopkins University Applied Physics Laboratory, 11100 Johns Hopkins Rd, Laurel, MD 20723, 2 University of California, Irvine, CA 92697-2625, 3 University of Kansas, Lawrence, KS 66045, 4 The Ohio State University, 191 W. Woodruff Ave., Columbus, OH 43210, 5 Jet Propulsion Laboratory, 4800 Oak Grove Drive, Ms 67-204, Pasadena, CA 91109, 6 The Lebedev Physical Institute of the Russian Academy of Sciences

Subject: NIAC Phase 1 Final Report: Using the Hottest Particles in the Universe to Probe Icy Solar System Worlds

1. ABSTRACT

We present results of our Phase 1 NIAC Study to determine the feasibility of developing a competitive, low cost, low power, low mass passive instrument to measure ice depth on outer planet ice moons, such as Europa, Ganymede, Callisto, and Enceladus. Indirect measurements indicate that liquid water oceans are likely present beneath the icy shells of such moons (see e.g., the JPL press release "The Solar System and Beyond is Awash in Water"), which has important astrobiological implications. Determining the thickness of these ice shells is challenging given spacecraft SWaP (Size, Weight and Power) resources. The current approach uses a suite of instruments, including a high power, massive ice penetrating radar. The instrument under study, called PRIDE (Passive Radio Ice Depth Experiment) exploits a remarkable confluence between methods from the high energy particle physics and the search for extraterrestrial life within the solar system. PRIDE is a passive receiver of a naturally occurring radio frequency (RF) signal generated by interactions of deep penetrating Extremely High Energy (> 10^18 eV) cosmic ray neutrinos. It could measure ice thickness directly, and at a significant savings to spacecraft resources. At RF frequencies the transparency of modeled Europan ice is up to many km, so an RF sensor in orbit can observe neutrino interactions to great depths, and thereby probe the thickness of the ice layer.

Prior to our NIAC Phase 1 study, we analyzed the capability of PRIDE under the assumption of pure cold Europan ice, which we describe in [9]. Our goal in Phase 1 was to evaluate the promise of the concept in more realistic conditions. We made considerable progress in multiple areas:

- We implemented several possible Europan ice models in detail, including impurity content and depth-dependent temperature and attenuation length. We identified a useful range of likely ice models for which event rates are in the hundreds or more per year and for which ice sheet depth measurement capabilities exist for thicknesses up to tens of km.
- We adapted three existing, higher fidelity simulations used in the EHE astrophysics community by the ANITA, RICE, and LORD projects to the PRIDE application, and compared results to validate our expected event rates and other measurables.

- We implemented models for several other ice moons: Ganymede, Callisto, and Enceladus, and implemented models for both Polar and Equatorial ice. We found that PRIDE is most promising for Europa and Enceladus, and that notably different depth measurement capabilities exist for polar vs equatorial ice due to colder polar temperatures.
- We implemented a model of local water inclusions within ice sheets. We found that a variety of local water inclusions for both Enceladus and Europa should be detectable, but should not significantly compromise our ice depth measurements
- We analyzed new observables to determine their ability to resolve ice depth independently of overall event rate, including event size, zenith angle to surface exit point and cascade location in the ice, and frequency content vs depth. We found promising results for some observables.
- We performed an initial analysis of cosmic ray events, which are expected to be a major background for PRIDE. We found potential measurable quantities to distinguish cosmic ray events from neutrino events.
- We leveraged existing efforts on developing low power digitizer technology to develop a chip applicable to PRIDE with 2 Gs/s rate, 1.3 GHz bandwidth, and expected favorable radiation hardness properties, which uses only 32 mW per channel, ideal for a deep space mission.
- We established an MOU with Russian EHE neutrino researchers at the Lebedev Physical Institute. They are now part of the PRIDE collaboration via their own funding, and have contributed modifications to and analysis with the simulation they developed for the LORD EHE neutrino project.

Table of Contents

2. INTRODUCTION

2.1 SCIENTIFIC NEED

2.1.1 Science Goals

We have conducted an initial exploration of a concept for a novel and innovative low cost, low power, low mass passive instrument to measure ice depth on outer planet moons, such as Europa, Ganymede, Callisto, and Enceladus. Indirect measurements by the Galileo and Cassini spacecraft indicate that liquid water oceans are likely present beneath the icy shells of such moons (see e.g., the JPL press release "The Solar System and Beyond is Awash in Water"). This has important astrobiological implications, and the exploration of such moons is a high priority. In particular, the ocean on Europa is thought to be a prime location for life to form outside of the inner planetary "Goldilocks zone" where the temperature is just right for planetary surface water to exist. The formation, structure, and evolution of these planetary objects are subjects of great interest for understanding how the conditions of life can form, and more generally for understanding the formation of these types of moons. The characteristics of the ice layer are important for deriving properties of the oceans underneath, and for planning future probes and determining possible locations for future landers. For example, on Europa the thickness of the ice layer is key to understanding the possible exchange of ocean nutrients with the surface, understanding the mechanism for heating the ocean, and determining whether the ice might be thin enough to allow a future probe to reach the ocean for sampling.

Currently, there is no easy way to measure the thickness of ice that could be tens of km deep, as doing so is very challenging given spacecraft SWaP (Size, Weight and Power) resources. The currently favored approach uses a suite of instruments, including a high power, massive ice penetrating radar (IPR), to provide constraints on ice thickness [21]. The described proposed instrument, which uses experimental techniques adapted from high energy physics, is a passive receiver of a naturally occurring signal generated by interactions of deep penetrating cosmic ray neutrinos. It could measure ice thickness directly, and at a significant savings to spacecraft resources. In addition to measuring the global average ice thickness this instrument can be configured to make low resolution global maps of the ice shell. Such maps would be invaluable for understanding planetary features and finding the best sites for future landers to explore. We describe the instrument concept and our analyses to date to determine feasibility. Our previous findings, prior to the NIAC effort, are also described in [9].

2.1.2 Relation to NASA Science Themes

The PRIDE instrument addresses each of the broad crosscutting themes of the 2011 National Research Council's Planetary Science Decadal Survey: building new worlds, planetary habitats, and workings of solar systems [23]. The first theme involves understanding solar system beginnings and one goal is to understand how giant planets and their satellite systems accrete. A crucial aspect is characterizing the internal structure of satellites orbiting giant planets, which PRIDE is uniquely capable of addressing. The second theme involves searching for the

requirements of life, and one goal is to understand whether contemporary habitats with the necessary conditions to sustain life exist beyond Earth. Priority has been given to searching for and characterizing modern-day subsurface habitats with access to liquid water. Mars, Europa, and Enceladus are recognized as having the greatest potential and, for the latter two bodies, PRIDE can provide information on fundamental characteristics of those possible habitats (e.g., depth to and thickness of a subsurface ocean). The final theme involves revealing the evolution of planetary processes through time; one ancillary goal is to understand how chemical and physical processes that shaped the solar system have operated, interacted, and evolved. Exploration of the hypothesized subsurface oceans of the three icy Galilean satellites, and Europa's hypothesized subsurface ocean in particular, are specifically called out as part of this goal. PRIDE can achieve this without the need for other supporting instruments.

PRIDE would also address a broad subset of questions associated with exploration goals described in the 'Satellites: Active Worlds and Extreme Environments' subsection of [23]. One goal is to understand how the satellites of the outer solar system form and evolve, and one objective is to understand how satellite thermal and orbital evolution and internal structure are related. Several important questions associated with this objective that PRIDE can address include: What are the thickness of Europa's outer ice shell and the depth of its ocean? Does Enceladus have an ocean or some other means of providing large tidal dissipation, and to what extent is its behavior dictated by its formation conditions (e.g., presence or absence of a differentiated core)? Another goal is to understand humanity's place in the universe by characterizing promising environments for the evolution of extraterrestrial life. An important relevant objective is to understand where subsurface bodies of liquid water are located, and what their characteristics and histories might be.

We also note that, owing to the fact that the icy moons have colder and thicker ice sheets than found on Earth, PRIDE may have the capability to detect more EHE neutrinos than any terrestrial neutrino project, creating a unique and exciting possibility for overlap with the Structure and Evolution of the Universe Roadmap [3]. We have been focused on measuring ice depth, but the possibility exists that with such a large neutrino detector we might see events that can be traced back to an astrophysical source, or could show an unorthodox energy distribution that would have implications for physics beyond the standard model of particle physics. Typical predictions of signals include only cosmogenic neutrinos from interactions of diffuse extragalactic cosmic ray nuclei with the CMB or with starlight. However other sources could exist, both point source (blazars, black holes e.g., [8A]) and diffuse (dark matter decays, relic topological defects see, e.g., [8B]). This instrument will have access to the largest target volume of ice in the solar system, and since the surface is covered with ice, unlike the Earth, full sky coverage. Point sources will show up as hot spots during a given orbit position/local time combination. Diffuse sources tend to have energy spectra that would peak at higher energies than the more conservative cosmic ray signal. Larger energy neutrinos will make a bigger pulse – and we could potentially detect these by looking at the distribution of events and determining if there are "extra" high energy events. Simulation of these exotic sources is simple; the interesting part of the exercise will be to see if we can modify the antenna and triggering pattern to better discriminate these events. One example of the types of changes we might expect: one model of particle dark matter decays preferentially into a tau type neutrino. Tau neutrinos produce tau leptons when interacting with ice, and the tau lepton almost immediately decays producing a

second shower. These "double bang" shows could be detected if we set up our triggering circuits to look for them. We have submitted an internal proposal at Johns Hopkins University with Marc Kamionkowski (an astro-particle physicist) to collaborate on surveying these potential exotic sources of neutrinos and properties of the resulting signals in the ice. Should this study be funded, we intend to incorporate the results, different triggering circuits in the simulation, so we can see if this can be a dual purpose (planetary/astrophysics) mission.

2.1.3 Relation to Past, Current, and Future Missions

2.1.3.1 Planetary Science Missions

PRIDE will build upon indirect measurements by the Galileo and Cassini spacecraft, which indicate that substantial liquid water oceans are likely present beneath the outer icy shells of a number of moons orbiting Jupiter and Saturn. As described above, PRIDE could provide an alternative or supplement to currently conceived future measurements of ice shell thickness on missions such as JUICE or a future NASA Outer Planet Flagship mission.

2.1.3.2 Astrophysics Mission Heritage

The methodology and detection technology used by PRIDE has already been demonstrated on several astrophysics and particle physics experiments. The details are described in the next section, following an explanation of the theoretical basis for the PRIDE concept..

2.2 TECHNICAL BASIS

The basic idea (see Fig. 1) is to use RF receiver technology to detect cosmic ray neutrinos passing through the ice and generating Cerenkov radio pulses. The sequence begins with a neutrino penetrating through the ice sheet at a grazing angle and interacting within the ice. Extremely High Energy (EHE - energies > 10^{18} eV) cosmic ray neutrinos are produced from the interaction of cosmic ray protons with cosmic background radiation [1]. Low energy neutrinos have very low interaction cross sections and are able to pass entirely through planetary bodies. At EHE energies, the cross section is high enough that neutrinos will not pass entirely through most ice moons, but will still penetrate deep into the ice or rock before interacting, if they arrive at grazing incidence angles. The interaction produces secondary charged high energy particles, which go on to interact and produce additional particles, leading to a shower of particles that moves through the ice for several meters. The shower will develop a net negative charge from both positron annihilation as well as forward scattered atomic electrons and, because it is moving faster than light in ice (c/n_{ice}), will emit Cerenkov radiation which is coherent at wavelengths comparable to its transverse physical size, up to ~0.2-2 GHz. The total emitted power is proportional to the square of the initial neutrino energy, and can be detected from orbit through a radio transparent medium such as cold pure ice. At Europan temperatures of ~50-100K attenuation lengths of tens of km or more are expected for pure ice, and up to several km for ice with impurities. The ice sheet thickness can then be determined from the various characteristics of the received signals, including event rate, direction, magnitude, frequency content, timing

characteristics, and polarization. The PRIDE instrument concept for observing these signals is a small array of low mass passive RF receivers read out by low-power, high speed digitizers (Switched Capacitor Arrays, or SCA's [2]). The basic concept of ice depth measurement was initially explored in Shoji et al [14] and Miller et al. [9], (based on our original idea [13]). In [9] we also laid out work needed to put the instrument on a more solid credible foundation – this will be discussed later. An appealing aspect of PRIDE is that it is low power by virtue of its passive operation. Table 1 shows a rough estimate of the resources used by PRIDE compared to an IPR.

The RF transparency of ice [24, 25] increases with decreasing temperature and varies with frequency and level and type of impurity. For cold ice, UHF (0.1-1GHz) is best, which matches the Askaryan Cerenkov emission spectrum very well. At Antarctic temperatures of -60C, appropriate for the ANITA [4] high altitude balloon project, the attenuation length expected from models at ~300-600 MHz is ~2-6 km, and has been measured to be > 1 km [26], allowing an RF sensor above the Antarctic ice sheet to observe pulses very deep into the 3 km thick ice. At Europan temperatures of 50-100 K, the modeled attenuation length is several times longer: 8-30 km at 100 K and 100-500 km at 50 K for the case of pure ice, though considerably less for impure ice. This makes it possible for an RF sensor in orbit to potentially observe neutrino interactions to depths of tens of km, and thereby to probe the depth of the entire ice layer. Due to refraction at the surface, most signals arriving at the satellite will travel fairly close to vertical before leaving the ice, so it should be possible to see signals from very deep ice sheets. Several authors have considered the composition of Europan ice and the effect of impurities on RF attenuation, generally in the context of an IPR operating at tens of MHz (e.g. [12, 30]). We describe below our analysis of the effect of impurities on ice depth measurement capability.

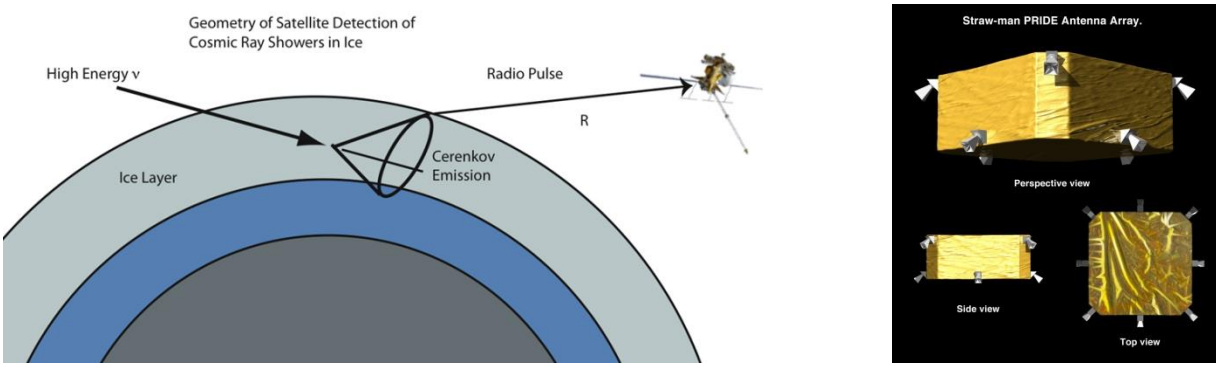

Figure 1. Left: The PRIDE concept. A high energy neutrino penetrates the ice at a grazing angle and initiates a shower of secondary charged particles that emit a detectable conical radio pulse of Cerenkov radiation. Right: Strawman PRIDE antenna array for full 360-degree azimuthal coverage. The two rings of antennas enable reconstruction of event direction via timing differences in neighboring receivers.

Table 1 Comparison of Active Radar and Passive PRIDE Parameters

	Ice Penetrating Radar [12]	PRIDE [9]
Dimensions (m)	10 by 3 by 2 array	30 x 20 x 70 cm horn antennas (3 to 8) 25 x 25 x 25 cm (600 MHz tripoles)
Mass (kg)	10	5-10 for array (ROM)
Power (W)	100	O(5-10) (ROM)
Frequency (MHz)	5-50	200-2000
Notes	Must self-deploy from spacecraft at site	No moving parts. Antennas placed at open locations on SC body.

2.2.1 Experimental Basis

2.2.1.1 Experimental Heritage

The detectable signal arises from an effect first noticed by Askaryan over 40 years ago. This Askaryan RF pulse has been demonstrated experimentally at particle accelerators [29,28] in silica sand, rock salt, and ice. Several other Askaryan Effect experiments have already been undertaken to detect high energy neutrinos, though using the approach to search for abodes suitable for extraterrestrial life is novel and unique. ANITA, an Antarctic balloon-borne experiment, is the most similar to PRIDE in concept and execution [27]. ANITA uses an array of about two dozen large horn antennas since (1) mass and power are far less constrained on a balloon flight than for PRIDE, and (2) on Earth, RF thermal and manmade backgrounds are higher, requiring additional channels and trigger logic. ANITA has demonstrated the viability of the concept via multiple circumpolar long-duration flights, including in January 2009 [4] and the most recent in December, 2014-January, 2015. Hoover et al. [8] describe the observation of 16 EHE cosmic ray events by ANITA during the 2006-7 campaign. While these events were initiated by cosmic rays, not neutrinos, such a successful observation still lends confidence to the viability of the Askaryan Effect technique for observing both cosmic ray and neutrino induced events from high altitude balloons and satellites. ARA (Askaryan Radio Array) is another under-ice radio array that has recently begun operation [5]. ARIANNA is a near-surface array in the early stages of deployment on the Ross Ice Shelf in Antarctica [6]. It also observes an ice sheet with liquid water underneath, and so detects reflected in addition to direct RF pulses. EVA [31] is a proposed successor to ANITA in which an overpressured high altitude balloon acts as a very large RF antenna, greatly increasing sensitivity. Additional past experiments include RICE [7] in Antarctica, and the satellite-based FORTE [33]. LORD is a proposed lunar orbiting satellite, similar in many ways to PRIDE, but observing RF pulses from neutrino events in the lunar regolith instead of ice [42]. While regolith is much less RF transparent, having an

attenuation length of only a few meters, the volume observed by a lunar satellite is still great enough to contribute to EHE neutrino astrophysics.

2.2.2 Measurable Quantities Related to Ice Sheet Thickness

In order to determine ice sheet thickness, we must relate those quantities that PRIDE can measure to depth or thickness. PRIDE has the capability to measure multiple quantities of both single neutrino events and distributions integrated over time, many of which could potentially indicate ice sheet thickness, as described below.

2.2.2.1 Event Rate

The simplest measurable quantity indicative of ice sheet thickness is the overall event rate. As the ice sheet thickness increases, the target volume visible to a satellite will increase and so will the corresponding observed event rate. However, this only remains true as long as the ice is clear enough that events continue to be visible from greater depths. In fact, the primary factor that will limit the depth to which PRIDE can measure thickness will be the transparency of the ice. In addition, the detection rate must be high enough for different ice depths to give different signals that are statistically significant. This can be an issue because the flux of neutrinos at such high energies is very low, which is why similar experiments observe very large target volumes.

We showed in [9] (see Previous Results below) that the event rate correlated with ice thickness for satellite observations for the case of pure cold ice, indicating that PRIDE may have depth resolution up to great thicknesses (> ~ 50 km). Shoji et al [14] also analyzed event rate vs ice sheet thickness and showed that ice thicknesses up to ~8 km could be measured for the case of dirty ice with a constant attenuation length of only 2 km. A primary goal of this NIAC effort was to establish that ice depth could be measured for realistic, detailed ice transparency models, including dependence upon impurity level and varying temperature with depth.

In addition, while event rate may correlate strongly with ice sheet thickness, there are currently large uncertainties in the flux of EHE neutrinos, and only neutrinos in the nearby PeV (10^{15} eV) energy neutrinos have been detected in ice [8A], not yet up to the EeV range of PRIDE. This could create large systematic uncertainties in the ice depth measurement. However, a number of experiments are currently underway to measure the charged cosmic ray and neutrino fluxes. By the time PRIDE arrives at Europa, one to two decades of observations should significantly reduce the uncertainty in the flux of neutrinos in the EHE range. For a review of current experimental efforts, see e.g. [34, 35]. Nevertheless, it is desirable to explore measurable quantities that are both indicative of ice sheet thickness and also independent of overall event rate so that any uncertainties in the neutrino spectrum will have less effect on the ice sheet thickness measurement.

While the primary goal of the design of the instrument as described herein is to characterize the ice on outer planet moons, we also know that this instrument would also be capable of making discoveries in astrophysics. The techniques we are using here come from astrophysics experiments that use Antarctic or Greenland ice sheets to learn about astrophysical sources of EHE neutrinos. The reason these techniques are used in Antarctica is that the flux of these particles is fairly low compared to say ionizing cosmic rays in the atmosphere, so large

target volumes of ice are needed. The reason it can be used here is that the target volume of visible ice can be orders of magnitude larger than a balloon observation of the Antarctic ice sheet. We are considering an instrument that is orbiting at a higher altitude over a thicker ice sheet and both of these factors contribute to a larger visible volume of ice (e.g. the Antarctic ice sheet is typically between 1-3 km). Also, a balloon over the Antarctic has a limited view of the sky, while a satellite that orbits a moon completely covered with ice can see the whole sky. If a particular source in the sky is bright in neutrinos, we will be able to see its Cerenkov cone of brightness from orbit. Also if there are exotic sources of very high energy particles, say decaying cosmic strings from an early phase transition, they will produce very bright neutrino showers and we ought to be able to detect them by their different distribution in event brightness (the signal is proportional to the energy of the event. With additional effort we may be able to see other features of events caused by relics from the early universe. For example a tau type of neutrino produces a tau particle, which quickly decays and produces a second shower. If we tune the electronics to look for this type of "double bang" event, we can determine the tau neutrino fraction. Some types of dark matter decays produce a higher fraction of tau neutrinos. If there is an unexpectedly large number of tau events, this could be a signature of dark matter. We are pursuing this possibility with astrophysicist Marc Kamionkowsky at Johns Hopkins University, to see if other sources could be detected with the PRIDE instrument.

2.2.2.2 Zenith Angle

Directional information can be extracted from detected events via time of arrival differences in different antennas. Timing differences among antennas at different altitudes on the spacecraft will indicate zenith angle, while differences among antennas at different locations on the circumference will indicate azimuth angle. The ANITA experiment [4] has demonstrated that signal timings can be compared to give directional information. The direction from the interaction point of each event to the receiver depends upon the depth of the interaction. If the zenith angle to the neutrino interaction point can be measured, and if events at all depths are equally likely to be detected, we would expect deeper ice sheets to form a zenith angle distribution with more events at greater zenith angles, while shallow ice sheets will form a distribution with more events very near the horizon angle. Thus the zenith angle distribution could provide a thickness measurement independent of overall event rate. In practice, however we expect that most events will cluster at zenith angles near the horizon. This happens because at such high neutrino energies the neutrino-nucleon cross section is high enough that most detectable events are due to neutrinos arriving at near grazing angles relative to the ice surface. In addition, the direction to the interaction point may not be directly observable. The direction to the point on the surface at which the RF pulse from each event exits the ice can be measured, but this will not be the same as the direction to the interaction point due to refraction at the surface. This will result in most events from all depths arriving in a narrow annulus near the horizon because refraction at the ice surface causes the detectable RF radiation to follow a path that is near to vertical in the ice, weighting emission points toward the horizon. This will make discrimination between different ice depths difficult based solely on the peak zenith angle of arrival challenging.

It is also worth noting that the measured zenith angles may actually be somewhere between the straight path to the interaction point and the path including refraction, due to surface roughness. Earth based radar measurements of Europa at 3.5, 13, and 70 cm wavelengths show that low temperature icy surfaces act as retro-reflectors, likely caused by a coherent backscatter effect related to sub-surface scattering by refractive index inhomogeneities [39, 40, 41]. This effect has also been observed for other icy surfaces in the solar system at both 13 and 70 cm wavelengths, and so may be important for the transmission of the Cherenkov emission through the upper surface layer of Europa. The transmission of electromagnetic waves through randomized rough surfaces like the case we are considering has been studied before. Dogariu and Boreman [38] have developed a model for photon transmission through rough surfaces with correlation lengths on the order of or larger than the photon wavelength. Features of this model have been verified in laboratory measurements by Griswold et al. [36] and Daub et al. [37] for surface roughness cases applicable to ANITA. They observed several features of the transmission that will have impact upon ANITA and PRIDE. First, the randomly oriented surfaces cause the angular distribution of the transmitted radiation to be broadened and the peak transmitted power to be reduced. Second, the peak transmission angle moves away from the Snell's Law refraction angle and toward a straight line path. Third, transmission becomes possible at incidence angles that would otherwise result in total internal reflection for a smooth surface. Griswold et al and Daub et al note that it is not immediately clear what quantitative effect this will have on the observed ANITA signal rate. Since the peak transmission power is reduced, the threshold of the receiver is effectively increased, which will lower the detection rate. However, the broadening of the transmitted beam will increase the effective angular acceptance of the receivers, increasing detection rate, and work is still underway to determine what the overall effect will be. In the case of PRIDE, the change in peak transmission angle from the refracted angle to an angle closer to a straight path may also make the measured zenith angle more sensitive to the depth of the interaction.

2.2.2.3 Azimuth Angle

It may be possible to determine variations in ice depth over the body of an ice moon by including reconstructed azimuth angle data. Most ice moons are expected to be colder near the Poles than at the equator, which would make the ice more transparent at higher latitudes. Variations of ice shell thickness with latitude are also possible. Shoji et al [11] showed that even a single omnidirectional antenna could be used to detect gross features in the ice. In their case, they simulate a south polar ice thinning that is suspected on Saturn's moon Enceladus. Because radio signals cannot propagate through water and propagate less through warm ice near water boundaries, they found that a count rate decreasing with latitude would indicate a region of thin polar ice. However, if instead we use more than one antenna and signal timing information, we could more precisely determine differential count rates and use that information to produce a low resolution map of global ice distribution. Figure 2 shows important potential features in the ice that could be determined by comparing differential count rates.

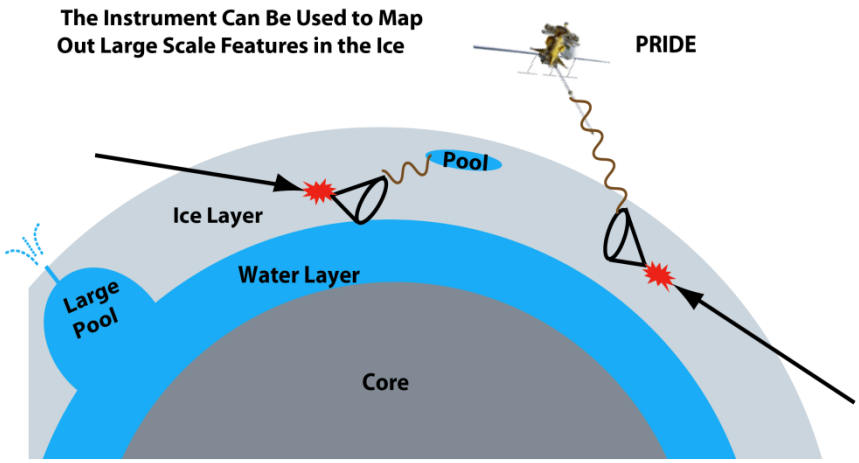

Figure 2. Features of the ice, especially water intrusions and embedded pools, will cause the count rates to vary in different directions. By assembling the global directional count rates, a low resolution map of the ice can be constructed.

2.2.2.4 Amplitude Distribution of Events

Another measurable quantity is the event amplitude at the receiver, measured in terms of either the peak voltage or total RF power. For a given or known neutrino energy, there is clearly a correlation between measured amplitude andevent depth, as events from greater depths will suffer more attenuation in reaching the receiver. However, since the emitted electric field amplitude from an event is roughly proportional to E^2, distinguishing small (lower neutrino energy) events at shallow depth from large (higher neutrino energy) events at greater depth is a challenge. One approach is to consider the amplitude distribution. If there is some maximum detectable neutrino energy, there may be fewer events with large amplitudes. Shoji [14] found a dependence of event amplitude distribution on ice sheet thickness. Miller et al [9] also found indications of a dependence, but with low statistical significance, so further exploration is needed.

2.2.2.5 Frequency Content of the Received Signal

Since the ice transparency is frequency dependent, the frequency content of detected signals will depend on the amount of ice traversed, and the relative power of received signals in different frequency channels should be indicative of the interaction depth for single events. This is an additional ice depth measure that can be simulated, but which had not been explored before the NIAC study.

2.2.2.6 Timing Difference for Direct and Reflected Signals

Measurement of signals reflected from the ice/water interface can also indicate ice sheet thickness, possibly from very few events. Down going signals can reflect off of the ice/water boundary and also be detected in orbit. It is therefore possible that we could detect the direct signal and some microseconds later the reflected signal. The time difference between the signals would indicate the length difference of the two paths, and thus yield an independent measure of the ice depth. If such events could be detected, a measurement of ice sheet thickness could be made on each individual event. We note that the ARIANNA instrument [6] intends to detect mostly reflected radio pulses at the bottom of the ice/water layer in Antarctica.

2.2.2.7 Timing Difference due to Birefringence and Polarization

Terrestrial polar ice has a different index of refraction for one polarization vs. the perpendicular polarization. If similar ice exists on ice moons, and the birefringent asymmetry can be determined or estimated, the time difference in arrival between the two polarizations (Cerenkov radiation is polarized) will indicate the path length through ice, again on individual events.

2.2.2.8 Multiple Quantities

Previously unexplored is the approach of using multiple measures on individual events. For example, one could measure timing differences due to both birefringence and direct/reflected paths, along with frequency content and zenith and azimuth angle and intensity to form a combined estimate of the depth of each event. This approach could also be used to discriminate neutrino events from background events such as cosmic rays or local RF pulses.

3. RISKS

We have yet not discovered any “show stoppers” that make PRIDE impossible, but there are multiple risks to the PRIDE concept that could possibly result in the instrument not being feasible or not being capable of making the desired depth measurement. In this section we discuss the most significant PRIDE risks. The investigations and analysis tasks to date have been oriented primarily toward efficiently reducing the most significant risks.

3.1.1 Event Rate

One risk is the event rate itself. EHE neutrino interactions in matter are very rare and require detectors with extremely large effective volumes. The ANITA experiment, for example, observes much of the Antarctic ice and expects to see on the order of only a single event or less per 20-30 day flight. In fact, to date terrestrial experiments have yet to detect a single EHE neutrino. An advantage of PRIDE is that it observes an extremely large effective volume due to its altitude and the depth of the Europan, or other ice moon, ice sheet. Initial investigations [9,

14] reported very high event rates, on the order of 10^4 events per year or more, which is considerably more than expected by the later predictions of high fidelity codes used in the EHE neutrino astrophysics community, even for very clear ice. This is not a surprise, as the simulation of [9], for example, was simplistic and used a simple power threshold for events, with no consideration of antenna directionality, additional background noise, or trigger inefficiencies. One of the primary goals in Phase 1 was to determine realistic expectations for event rates and verify that they should be high enough to make accurate ice depth measurements, including possible local variations in ice depth.

3.1.2 Ice Impurities and Complex Ice Effects

Impurities, defects, and surface roughness of the icy shell can degrade the expected signal to the extent that we cannot determine ice thickness. Our initial analysis assumed very cold pure ice as a most optimistic initial case. We expect that the limiting factor in RF ice transparency will be due to impurities, and that the event rate and maximum detectable depth will be reduced, possibly considerably, when impurities are considered. In Phase 1 one of our primary goals was to investigate more realistic ice transparency models, including impurities and changing temperature with depth, in order to determine if high enough event rates and useful depth measurement capability remained in the presence of more realistic ice models.

In addition, at pressures exceeding 200 Mpa, corresponding to roughly 21.2 km ice depth, there is a phase transition from the familiar Ice Ih to either Ice III (-30 C<T<-20 C) or Ice II at temperatures less than -30 C, although Ice II has been more readily synthesized in the lab from Ice V. Owing to the high pressure and the corresponding close packing of the ice molecules, the density in both these phases is approximately 25% higher than that of Ice Ih, which will lead, again, to some internally reflected signal, and therefore enhanced acceptance for downwards-directed Cherenkov radiation. Similarly, at depths exceeding 60 km, there will again be a phase transition to Ice V, having a density approximately 10% higher than Ice III or Ice II. The magnitude of these effects have not yet been evaluated, but will be studied over the course of Phase 2.

3.1.3 Cosmic Rays

Another important risk is that background charged cosmic ray cascade signals may not be effectively distinguished from the neutrino pulses. Charged EHE cosmic rays impacting on the surface of an ice moon will initiate cascades that produce RF pulses in the same manner as neutrino-initiated cascades. Events due to cosmic ray nucleons appear to be a major background source for current Antarctic balloon neutrino pulse detection experiments, and this noise source must be explored in detail.

In order to determine ice thickness with neutrinos, we need to find a way to exclude the charged nucleon events. However, we expect there to be at least three ways to possibly distinguish cosmic ray events from neutrino events. First, the cosmic ray flux is much better known and will be independent of ice depth, as all cosmic ray events impact upon the surface. This will result in a predictable constant addition to the total number of events, which can be

subtracted away, leaving behind additional noise due to increased fluctuations in the total event rate. Second, the statistical distribution of zenith angles should be different for cosmic ray events and neutrino events due to the different arrival geometries. Third, the pulse shape, polarization, and frequency content of cosmic ray signals is expected to be different because cosmic ray events are dominated by hadronic interactions, making them much more contained spatially, so we would expect cosmic rays to produce very impulsive signals while neutrinos would produce structured pulse trains. In addition, cosmic ray events should show no preferential absorption of higher frequencies due to shallow depth. We also note that it is possible that cosmic rays could potentially provide better measurement for shallow ice sheets (via reflections from the bottom) while neutrinos provide better measurements for deep oceans, making cosmic rays a possible asset if they can be identified.

3.1.4 Impulsive RF Noise Sources

There are several sources of background to consider, including thermal background from the ice moon itself, thermal and burst emission from Jupiter or Saturn, RF noise from the galactic plane, solar radio bursts, and RF pulses initiated by nucleonic cosmic rays striking the moon's surface. The background due to thermal emission is roughly the thermal energy divided by the effective antenna area kT/A. In the case of Europa, the receivers will be observing ice at ~50 to 100 K. Assuming an effective receiver area of 0.25 m^2 results in a noise estimate of ~5.5 X 10^5 Jy. In our previous work [9] we followed the procedure described in [4] to calculate the RF signal, adapted to an example Europan geometry, which resulted in a typical expected signal flux of F_{peak} = 6 X 10^6 Jy for an incident 10^{19} eV neutrino detected by a satellite, resulting in an SNR ~10, assuming that total noise is dominated by thermal noise. More realistically, there will be a contribution from system noise that to first order is probably comparable to the thermal noise, effectively requiring a higher SNR threshold for detection relative to the thermal noise floor. Note that because the energy radiated depends on the square of the number of particles, the signal strength goes roughly as the square of the energy of the primary particle, so SNR increases rapidly with increasing neutrino energy.

Local RF noise is produced by several sources in the Jupiter environment, and graphs of the RF background can be found in Carr et al. [22]. At tens of MHz or less, there is considerable burst emission, and at more than a few GHz there is thermal emission from the planet. Short transient radio bursts may produce false triggers but are unlikely to have the spectral characteristics of a Cerenkov burst from an Askaryan shower. These differences could be distinguished during data processing on the ground, and correspond to trigger rates which will be small compared to our maximum throughput At frequencies of ~100 MHz to a few GHz, the dominant local Jovian noise source is synchrotron emission from electrons in Jupiter's magnetosphere. However, this source produces much less noise than the burst or thermal emission sources, and fortuitously matches the same range of 0.2 to 2 GHz that is optimal for both Cerenkov emission and ice transparency. The values in [22] imply a maximum flux in the 0.2- to 2-GHz waveband at Europa of ~5 X 10^6 Jy at 800 MHz. This is about equal to the signal level calculated above, or 10X the expected background from thermal noise for the above antenna assumptions. However, this background is also directional and should be considerably reduced because it will primarily enter the antennas from off axis. While we expect galactic RF

noise and solar radio bursts to be less than the Jovian RF noise, these sources still need to be examined in detail. Strategies for rejecting local noise sources via directional sensitivity, direction reconstruction, and matched filter triggering using SCA's will need to be considered.

3.1.5 Surface Roughness

As discussed earlier, another important effect is at play when observing the icy planetary surfaces, namely that they are not smooth. The uneven surfaces cause a refraction of the radio waves that tends to smear the direction of the outgoing wave as it passes through the array of angles at the ice/space interface. This effect was discussed briefly in [9], but warrants a more thorough treatment in the simulation. The icy surfaces can be parameterized by a characteristic length scale (L) and an rms slope angle σ. These parameters have been estimated for some of the moons from visual imagery [e.g., see [15] for characterization of Europa and [16] for Ganymede]. This effect is important to include in our simulations in order to determine the resolution possible for the tomography of the ice shell. We note that this a major area of investigation for terrestrial EHE neutrino projects as well. PRIDE collaborators at University of Kansas are currently researching this topic for ANITA via a simulation they have recently developed and data that has been taken in 2015 using the HiCal balloon, and we hope to adapt the analysis to PRIDE in Phase 2.

3.1.6 Power Requirement and Radiation Hardness of fast Digitizers

Another notable challenge is fast sampling and digitization. The Askaryan signal is a short bipolar burst only a few ns in duration, as illustrated in Figure 3, requiring sampling rates of ~1-3 GHz to capture and reliably identify. Commercial fast ADC's capable of these rates require on the order of 10 W/channel, which is not feasible for an Outer Planet mission. A potential solution is Switched Capacitor Arrays (SCA's), described in [2, 43, 44], which have been used on other high energy physics and cosmic ray physics experiments, such as ANITA, with similar sampling and power requirements. SCA's enable considerable power savings, with each channel requiring only tens of mW [2]. SCA's have a slow readout, but this does not cause noticeable dead time because the event and random trigger rates should be very low. New generations of SCA's also include onboard triggering, in which several samples (a few ns deep) are sampled continuously, just long enough to form a trigger, at which point the rest of the SCA is read out. Triggering schemes include options to require both a high and low threshold on each channel, which could considerably reduce false alarms and increase sensitivity by reducing SNR threshold requirements, as Askaryan RF pulses are bipolar, while thermal fluctuations generally will not be.

Although SCA technology is amenable to Gsps sampling rates, and has been implemented on other projects, its newness in space environments poses some questions about radiation hardness, charging effects, and upset survivability. Kleinfelder (private communication) expects current SCA designs to have a radiation tolerance of ~1 Mrad or more, which could be increased to 10 Mrad or more via careful design.. Further effort is still needed to study any potential vulnerability in detail.

One effort under Phase 1 was to investigate the feasibility of developing SCA's especially suited to the PRIDE application in terms of power usage and triggering capability. In Phase 2 we hope to continue this investigation, in addition to determining SCA radiation susceptibility.

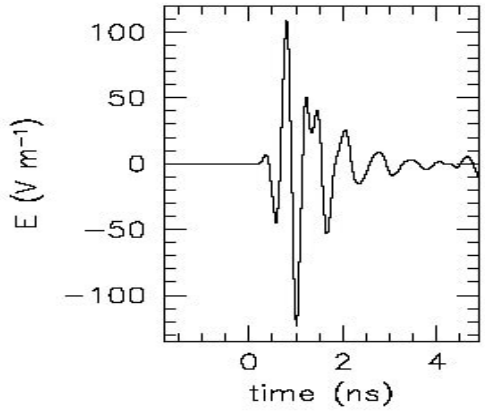

Figure 3: Example time domain Askaryan pulse. Shown is the time-domain signal for a well-matched receiver observing the signal at the Cherenkov angle.

3.1.7 Antenna Size

Another hardware risk is that the antenna and the array configuration needed for the signal sensitivity and exclusion of background noise could require larger, more massive structures on the spacecraft than can be accommodated. The primary requirements for the PRIDE antennas are that they have a fairly wide frequency range within the 0.2-2 GHz interval, have an antenna pattern with a wide enough angular acceptance to enable considerable overlap between multiple antennas facing different directions on the spacecraft (though the ability to reject pulses from undesired directions would be beneficial in order to reduce directional noise sources, including other instruments on the spacecraft), and be very light weight, on the order of only 5-10 kg for an entire multi-antenna array. In [9] we considered a straw-man antenna design based upon a commercial starting point, modified for the PRIDE application. The wide bandwidth used in the simulated signal calculation could be achieved with a ridged horn antenna. The final estimated antenna dimensions were 35 cm by 72 cm by 8 cm, with a mass of ~1-2 kg, which should meet all the requirements given above. Another promising possibility are the very low mass log-periodic Yagi antennas being considered for ARIANNA.

In general, larger antennas have the advantage of being more sensitive to lower frequencies, where ice attenuation lengths are the longest, but are also likely to have higher mass and thus be harder to accommodate on a spacecraft. Smaller antennas will be less large and massive, but may not have the required frequency range or sensitivity to carry out the measurement. In our previous analyses we assumed small (0.25 m^2) antennas, but did not take into account any loss of sensitivity at lower frequencies, so the combination of antenna size and

sensitivity required remains a risk to be investigated. Trade studies are required for the next level of design.

4. PREVIOUS RESULTS

In [9] we created a simple Monte Carlo simulation of the detection process, including the signal and thermal noise described above, in order to examine basic ice depth resolution capabilities. As an example of potential depth resolution, we show below the simulated event rate vs. ice sheet thickness for a satellite orbiting Europa in the case of pure ice and briny ice attenuation values, as given in [25]. As shown in Figure 4, the overall event rate is strongly dependent upon ice sheet thickness, indicating that PRIDE may have the potential to resolve ice sheet thickness to great depth, which would add value to any Europan, or other ice moon, instrument suite. However, it is clear that the maximum depth to which ice thickness can be measured is strongly dependent upon the level of impurities present in the ice, as the event rate continues to increase past more than 50 km depth for the case of clear ice, but levels off after ~20 km for the case of briny ice. This made it clear that studying the effects of detailed, realistic levels of ice impurities was of high priority in Phase 1. In addition, we found indications, though with low statistical significance due to our limited number of Monte Carlo events, that the measured zenith angle and event intensity distributions are also possibly dependent upon ice sheet depth, indicating that multiple observables may be combined to further specify ice sheet thickness, which is especially important if unknowns in the absolute EHE neutrino flux or attenuation length due to impurities make it difficult to determine the ice thickness from the detection rate alone.

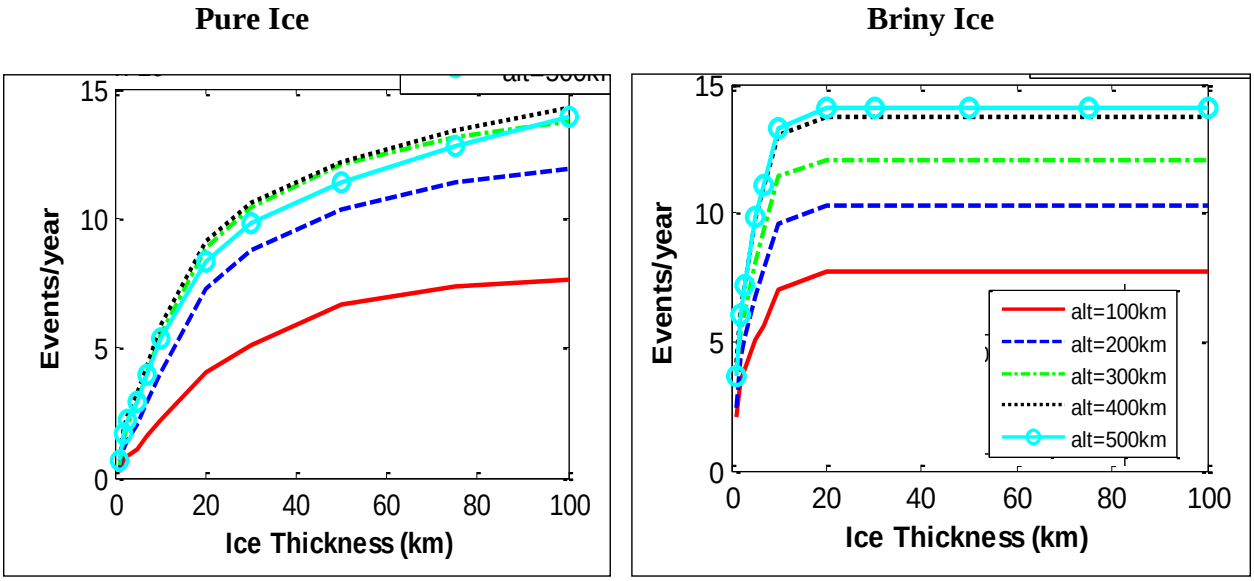

Figure 4. Illustration of simulated PRIDE results. Events/year detected vs. ice sheet depth. Left: pure ice. Right: briny ice. Neutrino energies are weighted by an E^{-2} spectrum. The detected event rate depends upon the ice thickness up to some maximum depth that depends upon neutrino energy and ice clarity. For pure ice, depths up to tens of km can be measured if the incident neutrino flux is known.

5. PHASE 1 RESULTS

5.1 PHASE 1 OVERVIEW

Our primary goals in the NIAC Phase 1 study were (1) analysis of risks that could make the concept impractical, in particular, would more realistic ice transparency models be a problem for PRIDE?, (2) demonstrating utility and promise by determining the maximum depth and spatial resolution possible, in particular including detecting varying ice thicknesses and large water pockets, and (3) hardware technology research and more detailed comparison, in terms of capability and mass and power requirements, to current approaches to perform the ice depth measurement. Our primary activity was to improve the fidelity of our Monte Carlo simulation in order to more accurately analyze the feasibility and capability of the concept, including implementing realistic models of the physical effects most likely to limit depth measurement capability via either reduction of signal or increase in noise. In addition to fidelity improvements, we made our simulation more general in order to analyze additional ice moons, including Ganymede, Callisto, and Enceladus, and to simulate and analyze the effects of variable ice thickness and water inclusions.

The large number of risks and potential measurements to explore made it impossible to examine every issue within the scope of Phase 1. The high priority issues explored in Phase 1 were: event rate, zenith angle, event amplitude, pulse frequency content, ice impurities, water inclusions, cosmic rays, and fast digitization. The issues remaining to be explored in Phase 2 include: azimuth/3D reconstruction, direct/reflected time difference, birefringence, polarization, multi-parameter analysis, radiation hardness, antenna/array optimization/trade studies, local RF noise sources, surface roughness, and mission design.

5.2 INTERNATIONAL COLLABORATION

We established an MOU with Russian EHE neutrino researchers at the Lebedev Physical Institute (LPI), who are now members of the PRIDE collaboration via their own funding, and have contributed analyses with the simulation they developed for the Lunar Orbital Radio Detector (LORD) EHE neutrino project (see below).

5.3 ADAPTATION OF EXISTING MONTE CARLO SIMULATIONS

Our initial simulation, PRIDEsim, which we describe in detail in [9], was very basic and made use of only simple, depth-independent ice transparency models. It did not take into account antenna directional response or triggering in multiple frequency bands, and assumed a very low SNR threshold. It predicted very high rates with depth measurement capabilities up to extreme thicknesses. It was expected that event rates would decrease when higher fidelity codes with more realistic effects were used. As shown in Figure 5, we replaced our simple simulation with three existing high fidelity Askaryan RF emission and neutrino propagation simulations that had been developed and tested over several years within the high energy neutrino astronomy community: the ICEMC simulation [10], the RICEMC simulation [7], and the LORD simulation [32]. As each code had particular strengths and weaknesses with respect to the PRIDE application, each can be used to investigate issues to which it is best suited. In Phase 1, we compared results between the codes to begin validating our expected event rates and other measurables.

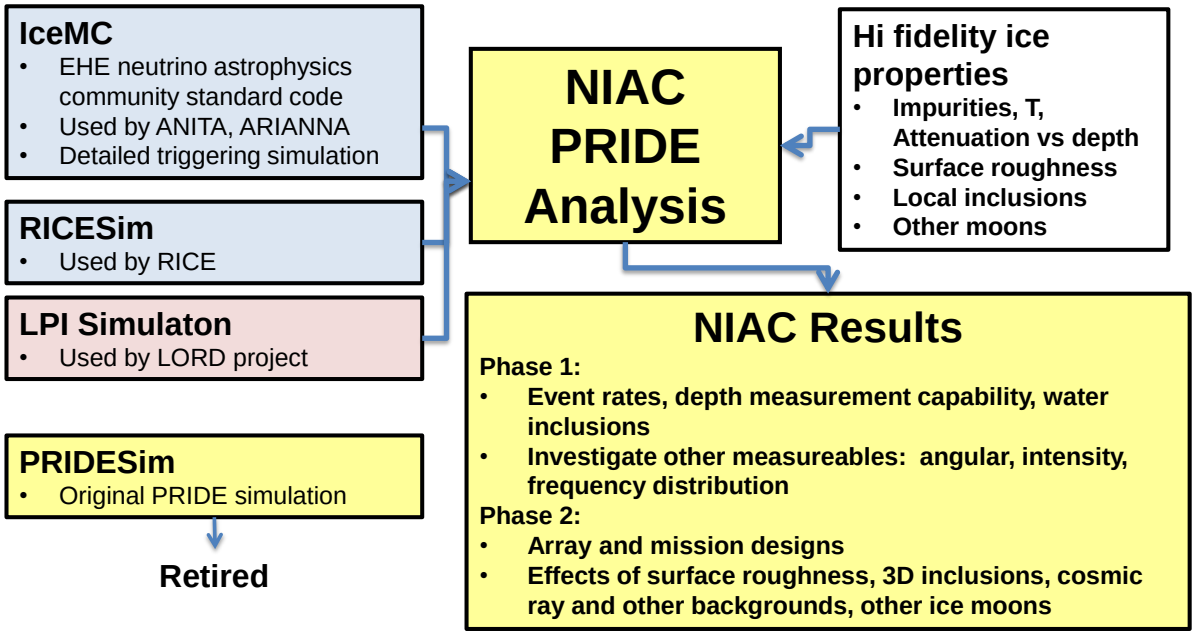

Figure 5: PRIDE NIAC Simulation Upgrade Plan. Our original simple simulation was replaced by three codes already used and tested in the EHE neutrino astrophysics fields, which were tested against each other for verification and validation.

5.3.1 IceMC

ICEMC has been adapted for and used to optimize ANITA, ARA, and ARIANNA, and has the capability to model many of the additional effects we desired: higher fidelity simulation of the Askaryan interaction, subsequent ray tracing, including changing index of refraction with depth, and signal magnitude at the antenna; multi-antenna arrays and triggering schemes; simulation of full time domain waveforms; simulation of thermal and electronics noise; configurable 3D planetary models and ice transparency models; higher fidelity propagation of neutrinos through rock, water, and ice; detailed calculation of event rates for multiple potential neutrino source spectra; reconstruction of event direction and magnitude from simulated measurements. Several members of the current PRIDE team have used ICEMC before on ANITA and ARIANNA, including adapting it to new project concepts.

We modified the configurable ICEMC parameters to produce versions to simulate all of the ice moons under consideration, and also extended ICEMC to incorporate significant planetary curvature effects. This required creating new versions of the planetary model (radius, distribution and density of rock, water, and ice layers), the ice transparency model, and the noise model (to include lower thermal noise due to the colder ice temperature). The antenna and payload/array model were more challenging to modify in the limited time of the Phase 1 effort, and were deferred until Phase 2. This allowed us to essentially fly the ANITA detector in orbit around Europa or other ice moons, which allowed us to examine:

- Relative aperture and event rates for Europa vs Antacrctica
- Ice depth measurement capability for a known EHE experiment
- Validation of apertures predicted by other codes

5.3.2 RICEMC

The RICE simulation is a frequency-domain based Monte Carlo, using the signal power spectrum prescription of Alvarez-Muniz et al., that was developed to estimate the neutrino sensitivity of the RICE Antarctic neutrino-detection experiment. After initial signal generation, thermal and system noise are added with frequency-independent, random phases. After accounting for ice attenuation and, in the case of PRIDE, Fresnel coefficients at the ice-air interface, signals are finally coupled to a distant receiver, where the frequency-domain spectrum is inverse Fourier transformed and, if the signal is 4 standard deviations above the expected ambient noise, a trigger signal issued. One feature of the RICE simulation is its emphasis on detailed ice modeling, including i) incorporation of birefringent effects, assuming a vertical c_axis and a 0.12% asymmetry in the wave speeds along the ordinary (assumed to coincide with the local ice bulk flow direction) and the extraordinary (perpendicular to the ordinary axis) axes. For the icy moons, it is unclear whether such a surface flow exists, so this feature has correspondingly been disabled, and ii) focusing of signal strength along optical caustics resulting from the variation in index-of-refraction of terrestrial polar ice with depth, which basically follows the density profile of ice with depth in Antarctica. Again, as the density profile is unknown for the icy moons, such focusing may be absent in our case. The ability to incorporate such effects is the strength of this simulation; its four shortcomings are: a) it calculates only effective interaction volumes and therefore must be externally married to a neutrino interaction model to calculate event rates, b) it has no provision for surface roughness or curvature effects at this point, c) it is assumed that the initial shower emanates from a single point; there is no current facility for staggering the time domain wave forms which would result from multiple in-ice interactions, and d) in general, it is an in-ice simulation which required retrofitting for the PRIDE application.

5.3.3 LORD MC

The LORD simulation was developed to assess the neutrino detection potential of a lunar-orbiting satellite. The Monte Carlo uses parametrizations of signal response and built-in Matlab functions to minimize execution time; a flexible steering file allows one to quickly evaluate sensitivity to frequency bandwidth, satellite elevation, ice thickness, neutrino cross-section, radio-frequency attenuation length, etc., and also generates a set of histograms which permit the user to quickly examine and verify the results of a particular simulation run. More subtle features such as water inclusions and surface roughness effects have yet to be included in this simulation. Perhaps the largest difference between the LORD simulation and the other simulations is that, in its default configuration, the LORD MC assumes a very large Jovian radio background, which, in its default configuration, results in a pessimistic estimate of the PRIDE sensitivity. Correcting for this effect, however, the LORD MC gives event yield estimates which

are generally commensurate with the other simulation packages. A sample image of some 3D event geometries for the LORD MC are shown in Figure 6, which illustrates the geometry used: the satellite is always above the north pole of the simulation coordinate system. To simulate water inclusions and other non-symmetric effects, the moon is rotated under the satellite, which remains stationary in the simulation coordinate system. In Phase 2 we will further upgrade the simulation to include arbitrary 3D satellite positions over a stationary moon with a full 3D ice transparency model, including local inclusions, and directional impulsive RF noise sources. In Figure 6 the angular acceptance of the antenna is apparent, as the detected events come preferentially from one direction. We will also upgrade the simulation to include multiple antennas facing arbitrary directions, and multi-antenna triggering.

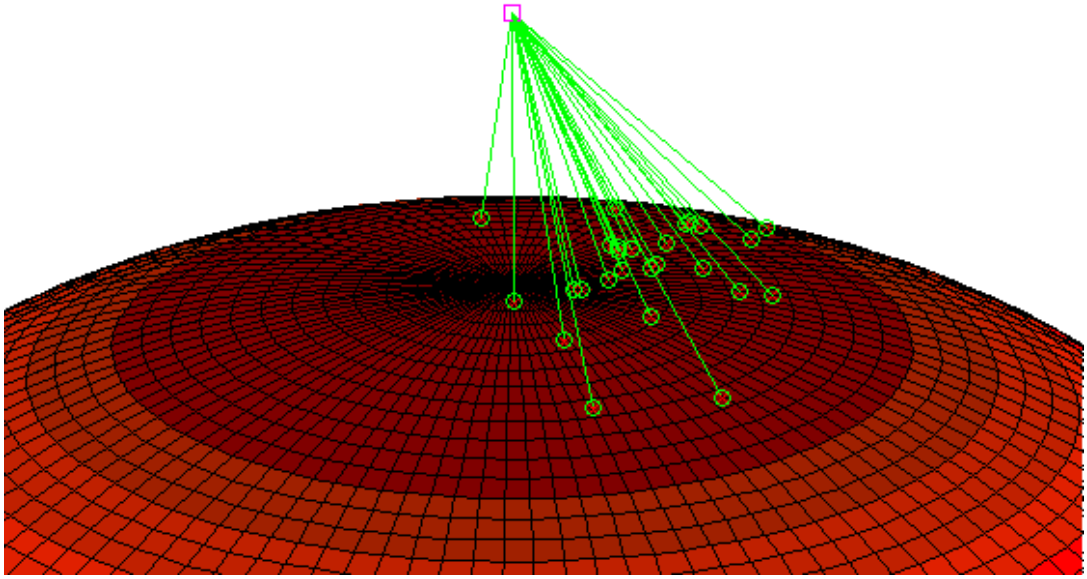

Figure 6: Illustration of sample LORD MC detected events. Magenta square = satellite location. Green lines = RF paths from ice surface to satellite.

5.3.4 Comparative Capabilities

Table 2: Comparison of capabilities, advantages, and disadvantages of simulations.

	PRIDEsim	**LORD MC**	**IceMC**	**RICEMC**
Depth dependent ice transparency, impurities	no	Yes (added in Phase 1)	Yes	Yes
Detailed antenna response	no	Yes	Yes	Yes
Multi-channel triggering	no	No	Yes	Yes
Detailed waveform simulation, time domain	no	No	Yes	Yes
Detailed waveform simulation, frequency domain	no	Yes	Yes	Yes
Cosmic rays	no	Yes	No (in progress)	Partially only
Detailed RF noise sources	No (thermal and system only, not impulsive)	No (thermal and system only, not impulsive)	No (thermal and system only, not impulsive)	No (thermal and system only, not impulsive)
Reflected events	no	No	Partially (not on same event as direct path)	Partially
Water Inclusions	no	Yes (added in Phase 1)	No	No
Surface Roughness	no	No	Partially	No

5.4 ICE TRANSPARENCY MODELS

We implemented several detailed Europan ice models, as described in [17,18,19], including both impurities and varying temperature with depth. We identified a useful range of likely ice models for which event rates are in the hundreds or more per year and for which ice sheet depth measurement capabilities exist for thicknesses up to tens of km. [17,18,19] describe three types of ice models, as illustrated in Figure 7. Marine ice consists of a thin ice layer, 1-3

km thick, over a deep ocean, with impurities dominated by sulfates from the ocean. Tidal ice consists of a variable thickness ice shell with impurities consisting of dust or salt. For both Marine and Tidal ice, the temperature increases from 50-100 K at the surface to 250-270 K at the ice/ocean interface. In convective ice models, a think rigid ice crust, 1-3 km thick, rests on top of a thick layer of convecting sea ice near the melting temperature. In this case, T rises from 50-100 K to 250 K within the thin rigid crust, the remains nearly constant through the thick convecting layer. Temperature and attenuation length profiles for all three ice models are shown in Figure 8 for an example ice thickness of 10 km. In our models, the ice impurity was characterized by a mixing fraction of lunar soil, the effects of which and probably concentrations are described in detail in [17,18,19]. A mixing fraction of 1% (*f=0.01*) is considered an optimistic but realistic case, while a mixing fraction of 10% (*f=0.1*) is considered a more pessismistic but also realistic case. Most of our analyses were performed for both *f=0.01* and *f=0.1* cases to test sensitivity to impurity level (optimistic to pessimistic realistic cases). In Figure 8 an *f=0.01* case is assumed. As can be seen, attenuation lengths are much shorter for convenction models due to their higher temperature at most depths. For thicker or thinner ice sheets, the temperature and attenuation length profiles will have the same shape but be scaled to correspond to the new depth according the temperature vs depth relation given in [17]:

$$T(z)=T_{surface}*\exp(z/(\text{thickness}/(\log(T_{base}/T_{surface}))))$$

One consequence of this is that thicker ice sheets will have longer ranges of ice with less attenuation because the temperature will be colder than at the same depth in a shallower ice sheet. This is illustrated in Figure 9, which shows the total one-way transmission at 1 GHz for a nominal model with impurity content consisting of 1% lunar soil, for ice sheet thicknesses of 3, 10, and 30 km. The Marine/tidal model with 50 K surface temperature and 10 km thickness has a total transmission from 10 km depth of ~10^{-3}, whereas the total transmission from 10 km depth in a 30 km thick ice sheet is ~4 x 10^{-2}, about 40X as much. This occurs because the first 10 km of ice in the thicker ice sheet is much colder on average. A consequence of this effect is that it could be possible to continue to observe higher event rates as ice sheet thickness increases even if events are not observable all the way to the bottom of the ice sheet, possibly increasing PRIDE's sensitivity at greater thicknesses. We note that an IPR does not have this advantage because IPR signals must always propagate through the entire ice sheet in both direction, passing through the warm ice at the bottom of the ice sheet twice, whereas for PRIDE, events only need to propagate one-way and so can continue to be seen from near the bottom of the ice sheet. This is further illustrated in Figure 10, which shows the maximum depth to which transmission is greater than 10^{-3}, as a function of frequency, for *f=0.01* ice in the left panel and *f=0.1* ice in the right panel. For ice sheets of 30 km depth, events are detectable at this level to >20 km depth in the nominal PRIDE frequency band of 0.3-0.9 GHz for *f=0.01* ice, and to ~10 km depth for *f=0.1* ice.

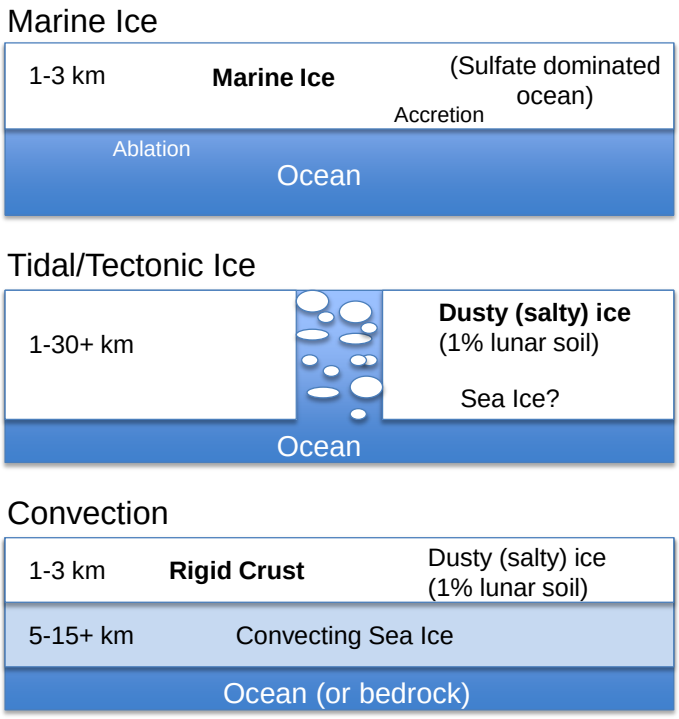

Figure 7: Types of ice models considered, from [17,18,19].

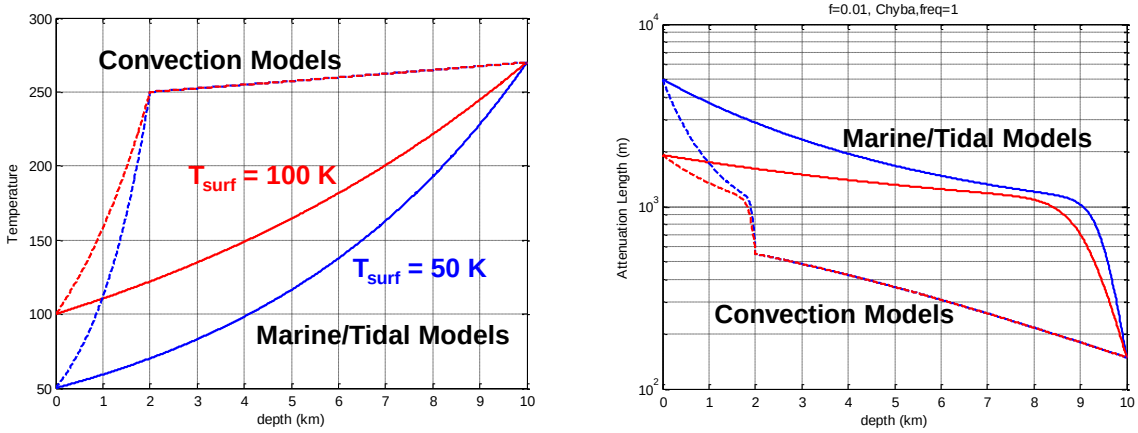

Figure 8. Left: Temperature vs Depth, Ice Sheet Thickness = 10 km. Right: Attenuation Length vs Depth: Thickness = 10 km, frequency = 1 GHz. Impurity Model = 1% Lunar Soil (f=0.01).

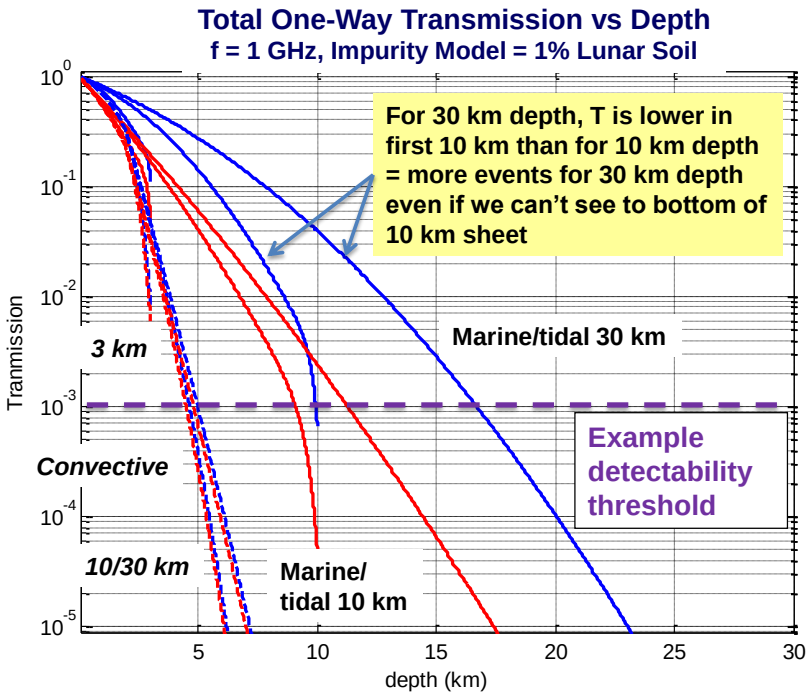

Figure 9: Left: Total transmission from given depth for various ice models.

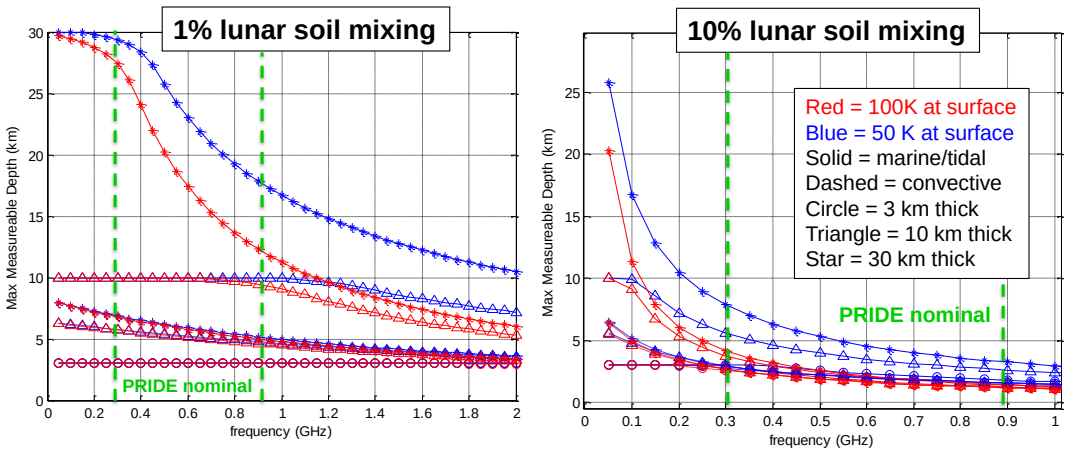

Figure 10: Maximum depth vs frequency at which events are detectable for various ice models, defined as depth at which transmission drops to less than 10^{-3}. Left: f=0.01. Right: f=0.1.

5.5 VERIFICATION OF EFFECTIVE AREAS

As described earlier, one issue is verification of event rates, which were predicted to be very high by the initial simple PRIDE simulation [9]. We expect the true rates to be lower due to ice impurities, but also due to lower detection efficiencies when higher fidelity simulations are performed. Historically, simple total power simulations such as [9] and [14] have predicted much higher rates than simulations that include detailed signals, noise sources, and detector responses. In general, taking 3 complicated simulations and trying to compare them is a non-trivial task, but the primary metric we need to compare is the Effective Aperture of the combined Moon-PRIDE system. We performed a comparison of predicted effective apertures between the three codes being adapted for PRIDE. One example is shown in Figure 11, which compares predicted effective volumes for ANITA by the RICE and IceMC codes, showing good agreement.

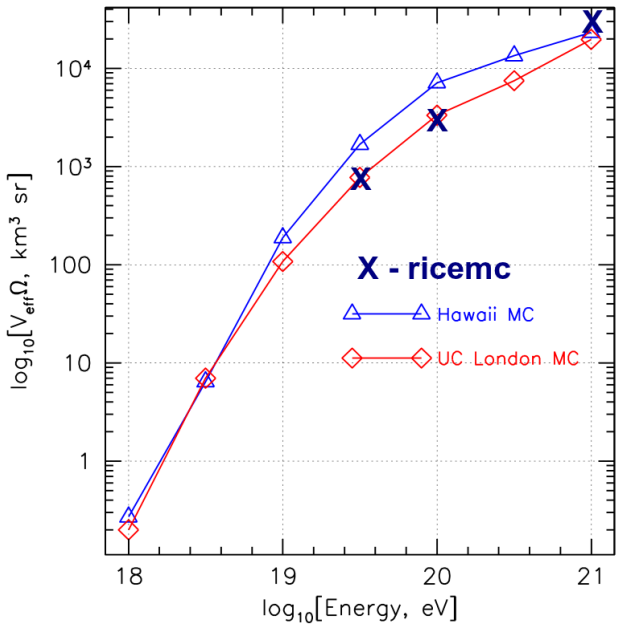

Figure 11: Comparison of RICEMC and IceMC effective apertures for Antarctic case.

A second example is shown in Table 3. Here several parameters were set to simple constant values in order to compare results between different codes. In this case the codes were two versions of IceMC, one modified at JPL previously to this PRIDE NIAC work, and one modified independently during the NIAC work at APL, and a modified version of the LPI LORD code. An Antarctic (ANITA-like) case was run with the detector at an altitude of 37 km observing ice of 3 km thickness and constant 1 km attenuation length, for three different neutrino energies. The results are shown in effective detector aperture in km^2sr, which is independent of

assumed neutrino flux. The first column shows the results for the JPL implementation of IceMC, while the second column shows the results for the APL implementation As can be seen, the results disagree slightly on energy threshold (represented by the large difference at 10^{19} eV,which is near the expected energy threshold) and by about a factor of two in sensitivity above threshold. The third and fourth columns show the results for the APL implementation of the LORD simulation, for SNR thresholds of 5 and 50. The SNR threshold of 5 predicts apertures about a factor of two to four higher than the higher IceMC result, while the SNR threshold of 50 agrees fairly well, though again with a slight disagreement in energy threshold. Our conclusion is that the SNR threshold of 5 apparently represents a more optimistic combination of overall triggering threshold and total background noise than is represented at higher fidelity in IceMC. In order to represent a combination of system and other external RF noise in addition to thermal noise, as well as multi-antenna and multi-band triggering and processing inefficiences, we will use a conservative SNR threshold of 50 for the LORD MC as our nominal value going forward, noting when excursions are made to other thresholds. Further work will be required to determine whether IceMC is overly pessimistic for the case of the PRIDE application, and what the appropriate SNR threshold should be for the LORD MC.

Table 3: Comparison of Event Detector Apertures, in km^{2}sr, between IceMC and LORD MC's, Antarctic Case

Log(E) eV	JPL IceMC, alt=37 km, Latt=1, depth=3	APL IceMC, alt=37 km, Latt=1, depth=3	APL LORD MC, alt=37 km, Latt=1, depth=3 SNR=50	APL LORD MC, alt=37 km, Latt=1, depth=3 SNR=5
19	15	0.4	5	20
20	60	120	125	400
20.5	200	400	400	1000

Next a Europan (PRIDE-like) case was simulated, with a satellite altitude of 200 km, 30 km thick ice sheet, and attenuation length of 10 km in the case of both APL simulations and 100 km in the case of the JPL IceMC implementation. The results are shown in Table 4. Here the two IceMC implementations agree fairly well once one is well above threshold energy, but the APL LORD simulation predicts about an order of magnitude higher sensitivity than either IceMC implementation. In the last column, the APL LORD simulation implementation was run for a noise floor of 218 K to explore whether the IceMC simulations might still be using an Antarctic ice temperature instead of the colder Europan temperature, but this did not account for the difference. So far we have not determined the source of this order of magnitude discrepancy for PRIDE, which did not show up in the case of an Antarctic scenario. Since the LORD

simulation was more easily modified and used for most of the rest of our analyses, further work will be needed in Phase 2 to determine whether the current results for the IceMC or LORD simulations are more accurate.

Table 4: Comparison of Event Detector Apertures, in km^{2}sr, between IceMC and LORD MC's, Europa Case

Log(E) eV	JPL Europa, Latt=100 km, d=30+, h=200km	APL IceMC, h=200 km, Latt=10, depth=30	APL LORD MC, 200 km, Latt=10, depth=30, t=110 K	APL LORD MC, 200 km, Latt=10, depth=30, T=218 K
19	40	0	30	0
20	450	100	4000	2500
21	1300	1500	10000	8000

5.6 EVENT RATE VS IMPURITY LEVEL AND SATELLITE ALTITUDE

A key finding from Phase 1 was verification that event rates may still be high enough to provide a useful depth measurement within a conceivable mission time (3 to 12 months). Example results are shown for Europa for equatorial and polar temperatures (100K and 50K) and for *f=0.01* and *f=0.1* level ice impurities, in Figures 12 (SNR threshold = 5) and 13 (SNR threshold = 50). The nominal settings for various PRIDE parameters used in this and most other results are shown in Table 5. There are several key takeaways from the results. First, the maximum measurable depth and event rate are strongly dependent upon both temperature and impurity level. We did not expect PRIDE to work in all possible conditions, as some ice models predict very high temperatures and impurity concentrations, leading to very little transmission. While event rates are detectable for even a pessimistic case (*f=0.1*,$T_{surface}$=100K), all observed events come from the first 1-2 km of ice, resulting in little depth measurement capability. However, even for *f=0.1* ice, at polar latitudes and temperatures there is still depth measurement capability to 25 km, and for more optimistic, but still realistic, impurity levels and temperatures, depth measurement capability exists up to tens of km.

Second, the maximum depth to which events can be detected is fairly independent of SNR threshold, apparently being dominated primarily by the ice conditions. The primary difference between SNR thresholds is in the event rates: the SNR_{thresh} = 50 results consistently have about four times lower event rates than the SNR_{thresh} = 5 results. This will have the effect of making the depth resolution coarser. For example, for the equatorial ($T_{surface}$ = 100), *f=0.01* case, at 400 km satellite altitude, for $SNR_{threshold}$ = 5, the number of events per year for a 3 km thick ice sheet is about 1400, while for a 10 km thick ice sheet the number is about 1800, a difference of about 9σ. In comparison, for the same conditions but for a $SNR_{threshold}$ = 50, the difference is about 350 vs 450 events in a year, or about 4.5σ. Note that these differences and

resolutions only include random statistical effects. We noted earlier that there are considerable uncertainties at present in the EHE neutrino flux, but we expect the spectrum to be much better measured by the time PRIDE would arrive at Europa, so in order to evaluate maximum potential we have only included statistical uncertainties in the above calculation.

Another key takeaway is the altitude dependence of the result. We simulated space craft altitudes from 30 km (to match Antarctic balloon cases) to 1000 km. Three key findings are:

1. Higher satellite altitudes are more effective than balloon altitudes at neutrino energies above ~10^{20} eV, at least for the neutrino spectra models we have explored. The longer ranges are offset by greater observed areas.
2. 300 to 500 km is always the optimal altitude, so a dedicated mission would ideally orbit at this altitude.
3. A wide range of altitudes are feasible, from ~100 to ~1000 km altitudes all having acceptable event rates. This implies that PRIDE could add value as an addition to a variety of missions, even possibly something like a Europa Clipper mission making multiple flybys at various altitudes.

This last takeaway is supported in Figures 14 and 15, which show results for effective aperture vs neutrino energy, satellite altitude, and ice sheet depth as determined by the IceMC simulation, but for a constant attenuation length of 10 km instead of the detailed ice models used in the LORD result. The same three trends for satellite altitude above are still evident for the IceMC results as well.

Table 5: Nominal PRIDE Values

Property	Units	Value	Notes
Antenna Area	m^2	0.25 or 0.6	Europa or Antarctica
RF Frequency	GHz	0.3,0.6,0.9	
Neutrino spectrum	GeV s-1sr-1cm-2	E^2dN/dE = 7e-8 or 5e-8	Mannheim or Waxman-Bahcall flux
Cosmic Ray Spectrum	1/(sec*km^2*ster*eV)	2e30*E^(-3)	
Hi, low Neutrino energies	Log10(eV)	18.5 to 21.5	
Ice impurity level	Soil mixing fraction	0.01 or 0.1	Optimistic vs pessimistic
Ice Temperature Profile	K	See Moons Table	
Ice Sheet Thickness	km	1 to 100	
Satellite Altitude	km	30 to 1000	(300-500 optimal)
Noise	K	50 to 218	thermal
SNR threshold	ratio	5 or 50	
Trigger	n/a	Total Power or 3 Frequency Channels	

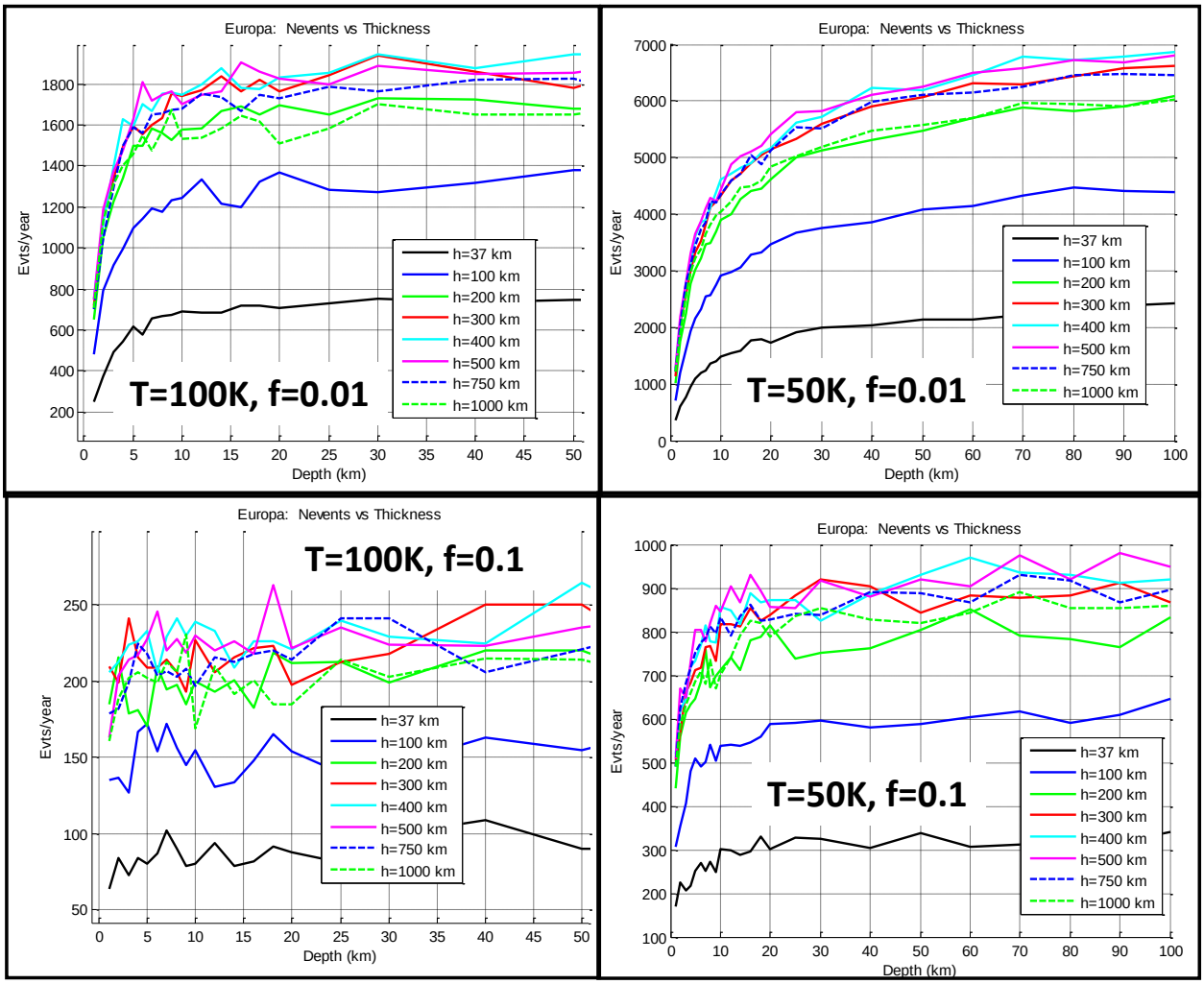

Figure 12. Europan neutrino event rates vs ice sheet depth for different surface temperature and impurity level, LORD MC simulation. UL: Equatorial ($T_{surface}$ = 100 K), f=0.01. UR: Polar ($T_{surface}$ = 50 K), f=0.01. LL: Equatorial, f=0.1 . LR: Polar, f=0.1. Threshold used was SNR=5. Event rates were reduced by about a factor of two to four for threshold SNR=5.

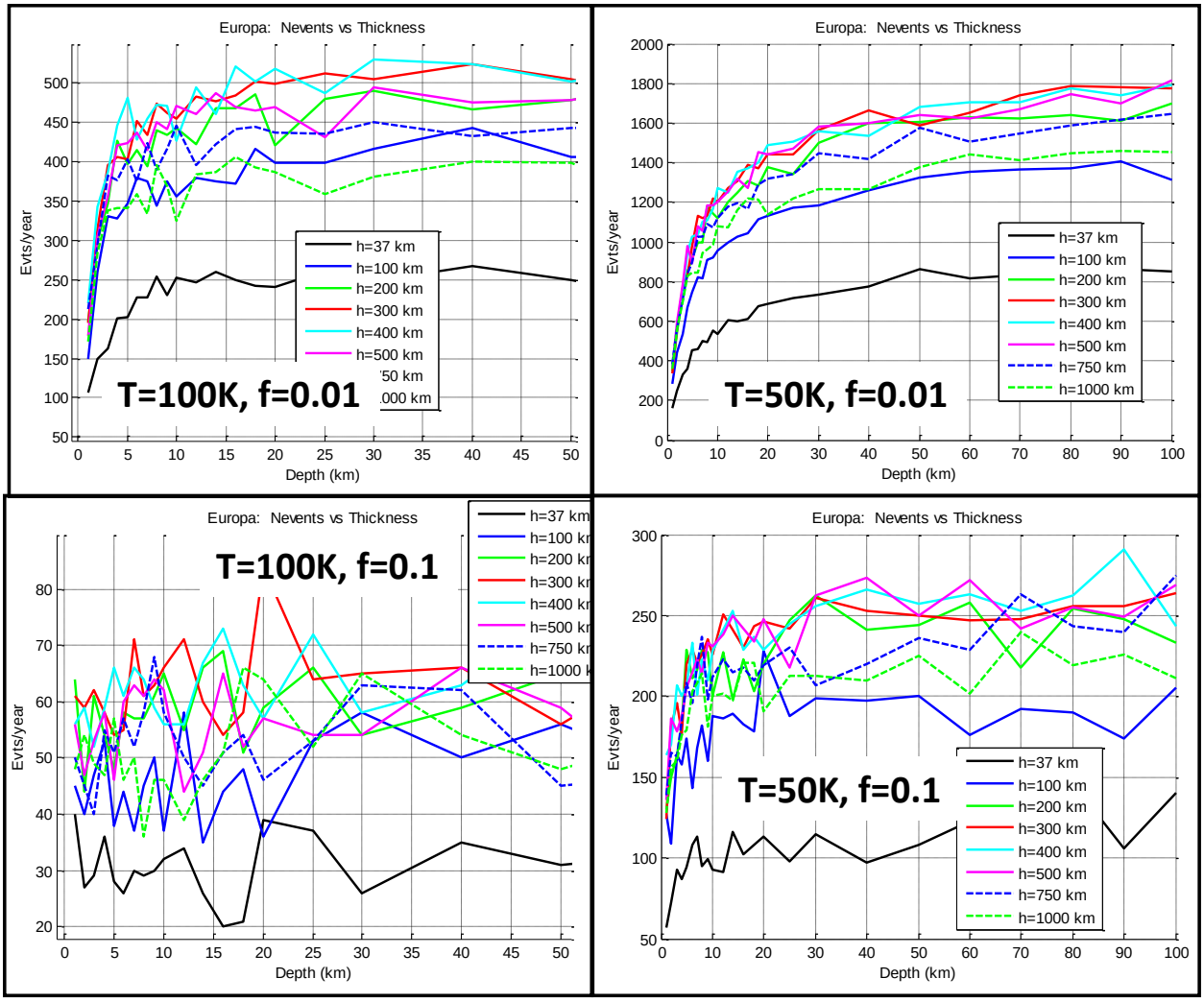

Figure 13. Europan neutrino event rates vs ice sheet depth for different surface temperature and impurity level, LORD MC simulation. UL: Equatorial ($T_{surface}$ = 100 K), f=0.01. UR: Polar ($T_{surface}$ = 50 K), f=0.01. LL: Equatorial, f=0.1 . LR: Polar, f=0.1. Threshold used was SNR=5. Event rates were reduced by about a factor of two to four for threshold SNR50.

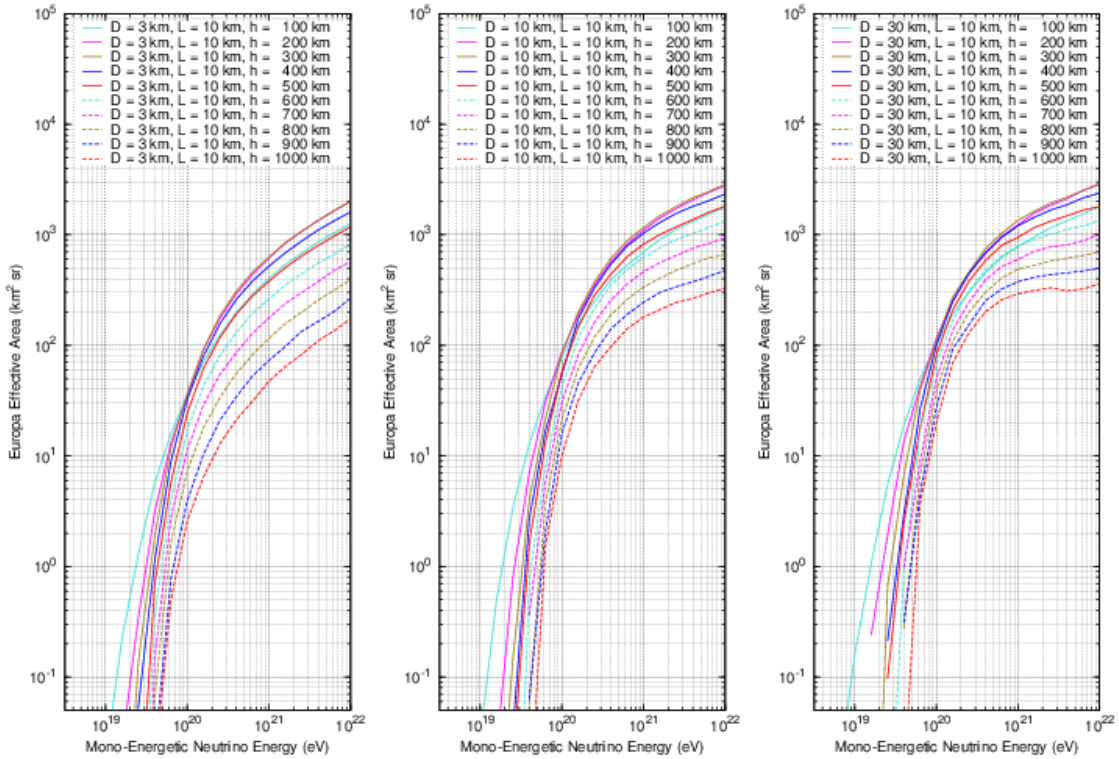

Figure 14. IceMC results for Europan neutrino effective apertures vs neutrino energy, for various satellite altitudes and and ice sheet depths. Left: ice sheet depth = 3 km. Middle: ice sheet depth = 10 km. Right: ice sheet depth = 30 km. RF attenuation length = 10 km in all cases.

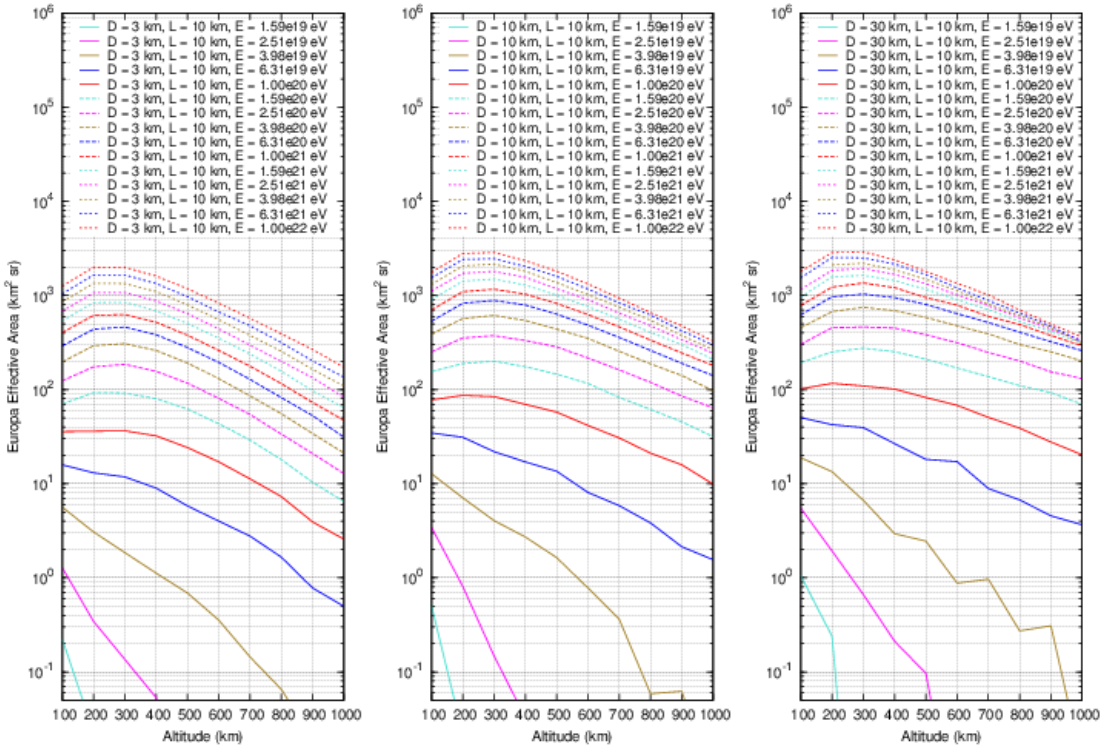

Figure 15. IceMC results for Europan neutrino effective apertures vs satellite altitude, for various neutrino energies and ice sheet depths. Left: ice sheet depth = 3 km. Middle: ice sheet depth = 10 km. Right: ice sheet depth = 30 km. RF attenuation length = 10 km in all cases. Peak aperture occurs at ~300 km in most cases, in agreement with the LORD MC simulation.

5.7 ADDITIONAL ICE MOON MODELS

We implemented models for several other ice moons: Ganymede, Callisto, and Enceladus, and implemented models for both Polar and Equatorial ice, in order to explore PRIDE's applicability to multiple missions. The models for the various moons, consisting of different radii and surface and bottom ice temperatures, are shown in Table 6. The results for Ganymede, Callisto, and Enceladus are shown in Figures 16, 17, and 18. A summary of the results for all moons is shown in Table 7. We found that PRIDE is most promising for Europa and Enceladus, and that notably different depth measurement capabilities exist for polar vs equatorial ice due to colder polar temperatures. The higher impurity mixing fractions were especially limiting for Callisto and Ganymede, though all moons showed both very high event rates and ice thickness measurement capabilities to >20 km for polar ice with *f=0.01* impurity

mixing fraction. This implies that PRIDE could have applicability to multiple ice moon missions.

Table 1: Models for multiple ice moons.

World	Radius (km)	Tsurface (Equator)	Tbase (Equator)	Tsurface (Pole)	Tsurface (Pole)
1. Earth	6371	218	270	200	270
2. Europa	1560	110	270	50	250
3. Ganymede	2634	160	270	100	250
4. Callisto	2410	135	270	80	250
5. Enceladus	252	75	270	50	250

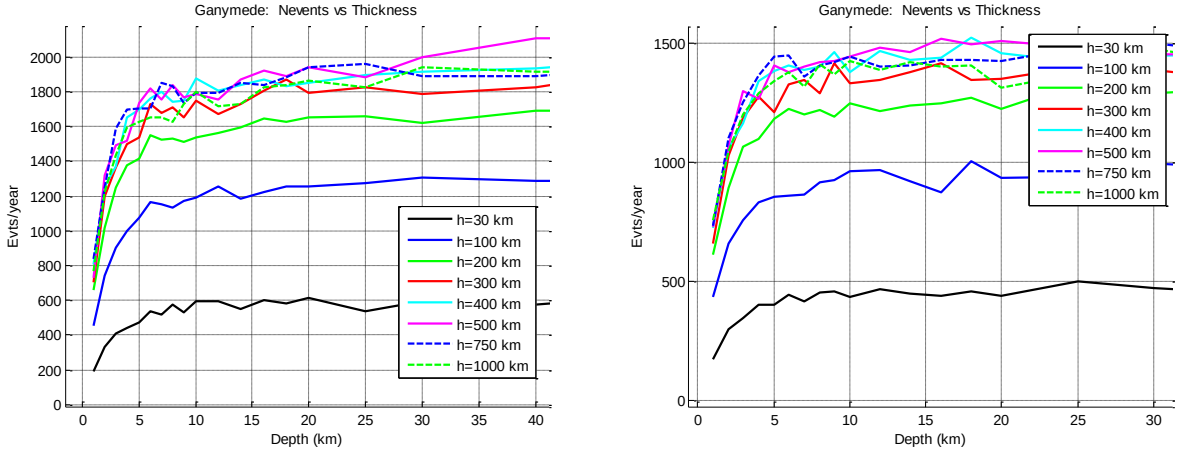

Figure 16: Event rate vs ice sheet thickness results for Ganymede. Left: polar ice temperatures, Right: equatorial ice temperatures. Ice impurity level = 1% (f=0.01), SNR threshold=5.

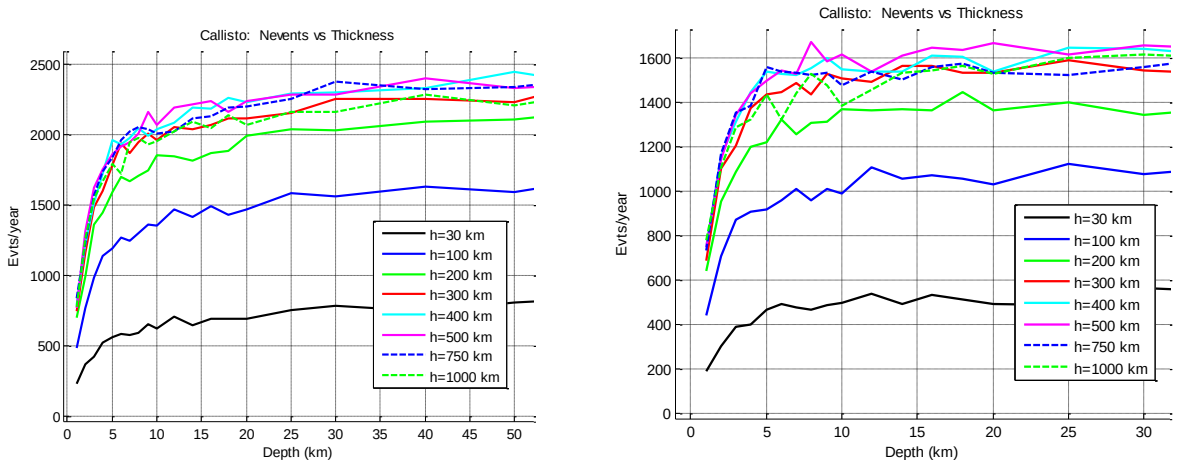

Figure 17: Event rate vs ice sheet thickness results for Callisto. Left: polar ice temperatures, Right: equatorial ice temperatures. Ice impurity level = 1% (f=0.01), SNR threshold=5.

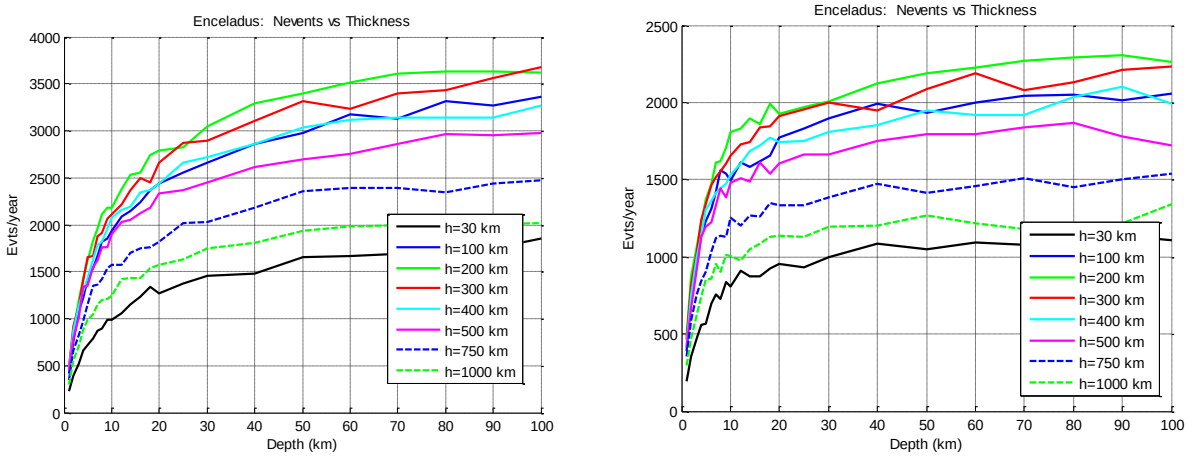

Figure 18: Event rate vs ice sheet thickness results for Enceladus. Left: polar ice temperatures, Right: equatorial ice temperatures. Ice impurity level = 1% (f=0.01), SNR threshold=5.

Table 7: Summary of results for multiple ice moons, shown as (maximum ice depth measurable/events per year for SNR threshold=5). Event rates are reduced by a factor of two to four for SNR threshold = 50.

World	Equator: f=0.01	Equator: f=0.1	Pole: f=0.01	Pole: f=0.1
Europa	20/2000	1/200	70/4000	25/600
Ganymede	10/1500	1/180	20/2000	2/250
Callisto	10/1600	1/200	30/2500	5/300
Enceladus	50/2000	10/200	80/3500	20/500

5.8 LOCAL WATER INCLUSIONS

As described earlier, another exciting prospect is the potential to sense large features in ice shells, as opposed to just measuring an average global thickness. An analysis using gravimetric data from Cassini flybys obtained from 2010–12 [20] implies that Enceladus likely has a non-global liquid water ocean beneath its frozen surface. The analysis suggests the top of the ocean lies beneath a 30-40 km thick ice sheet, and that the ocean is on the order of 10 km deep. It is not certain if the ocean exists only in the south polar region, stretches to the equator, or into the northern hemisphere, but it appears to be thickest in the south polar region and to extend to at least 50 degrees south latitude. Its existence also implies that the ice beneath the South Pole may be warmer than other regions, possibly by ~100K. Shoji et al [11] showed that even a single omnidirectional antenna could be used to detect gross features in the ice at Enceladus. In their case, they simulated a south polar ice thinning and conducted a parametric study over various ice thicknesses and ocean depths. Because radio signals cannot propagate through water and propagates less through the warm ice near a water layer, they found a count rate decreasing with latitude that indicated a region of thin polar ice.

We implemented a model of local water inclusions within ice sheets, and found that a variety of local water inclusions for both Enceladus and Europa should be detectable by PRIDE. At this point our simulation is still cruder than desired because we only simulated decreased count rates due to RF propagation paths through the ice being blocked by the water inclusions. We did not include the important effects of (1) the ice being warmer above the water inclusion due to the temperature vs depth profile changing locally to match the local ice depth, which would cause shorter attenuation lengths in the regions around the water inclusion and thus further reduce count rate, or (2) detection of reflections from shallow inclusions which would indicate shallow depth via their geometry. We will be able to simulate both of these additional effects in Phase 2 after improving our simulations to include full 3D models of ice depth and temperature over the entire ice volume. We simulated several inclusion cases resembling both the broad

shallow ocean of [20] and more localized hemispherical inclusions more closely resembling those studied in [11]. An example is shown in Figure 19 for the case of Enceladus with a 50 km thick ice sheet, a hemispherical inclusion that comes within 1 km of the surface, and *f=0.01* ice impurities. The inclusion is modeled as a sphere of radius 40 km with center 41 km below the ice surface. Any RF rays passing through the inclusion sphere are assumed to be blocked and are removed from the data set. The upper hemisphere that intrudes into the ice blocks many events that would be detected, while the lower hemisphere that is below the bottom of the ice has no effect on the simulation. All inclusions were modeled in this manner. The graph on the right shows detection rate vs latitude and altitude. The black line representing 30 km altitude shows a count rate that drops from 1600 per year near the equator to 1300 near the Pole, or about 7σ. At 100 km altitude the count rate drops from 300 to about 2800, a change of about 4σ.

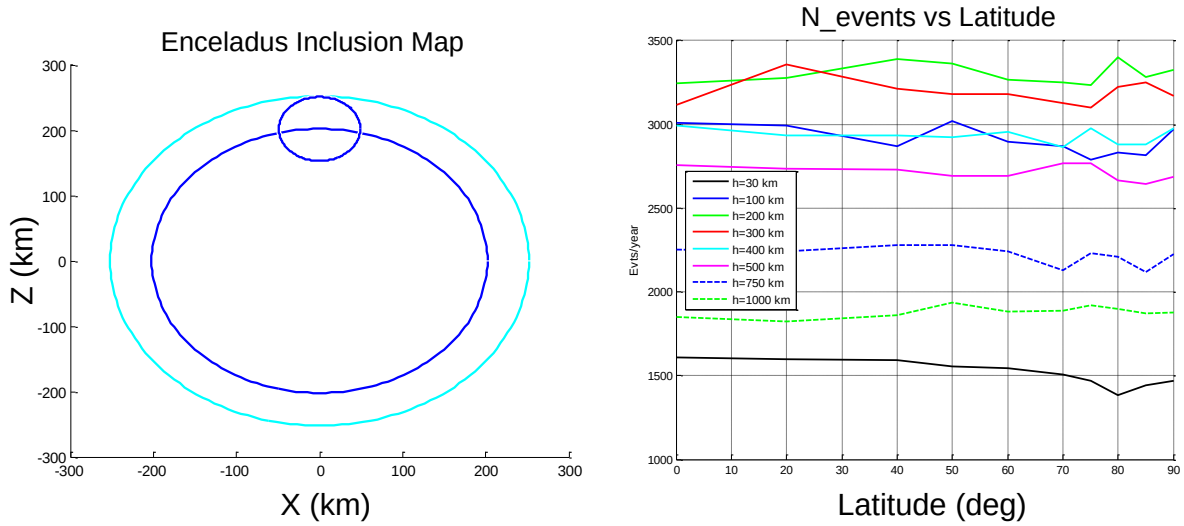

105

Figure 19: Example local Enceladus inclusion and event rates vs latitude for various satellite altitudes. Left: illustration of inclusion. The light blue line is the ice surface, the larger dark blue circle is the bottom of the ice layer, and the smaller dark blue circle is the outline of the inclusion, modeled as a simple sphere. The top half of the sphere intrudes into the ice layer, blocking RF ray paths. The bottom hemisphere of the inclusion is inside the rocky core and has no effect on the simulation. Right: Event rate vs latitude of spacecraft.

Figure 20 shows another case for Enceladus, this time more like the broad underice ocean described in [20], but coming to within 1 km of the surface of ice that is 40 km deep elsewhere (essentially creating a very local area of thinner ice). The inclusion is modeled as a sphere of radius 175 km, with center at a depth of 176 km. As can be seen, this creates a very broad but shallow underice ocean over much of the southern hemisphere. The detection rate results are again shown on the right. In this case, the ocean would be detectable at satellite altitudes up to 400 km. For both the small local inclusion and the larger broad ocean, we moved the inclusion center deeper and deeper parametrically to determine how deep below the surface it could be

detected. We found that broad inclusions could be detected via differential count rate on Enceladus in *f=0.01* ice at depths of up to 5-10 km and small local inclusions could be detected at depths of up to 1-5 km, using our current inclusion model. The optimum satellite altitude for detecting inclusions was generally lower than that at which the total count rate was maximized, with the event rate difference due to the inclusion often being lost if the satellite altitude was greater than 100-200 km. Figure 21 shows a less successful case that more closely matches the precise situation described in [20]. In this realization, 40 km thick ice contains a water inclusion of maximum thickness 10 km and minimum depth below the ice surface of 30 km, stretching for much of the southern hemisphere, much as described in [20]. The ice is modeled as impurity level *f=0.01*. The resulting count rate vs altitude is shown to the right, which is very nearly constant, showing only small dips at 30 and 100 km altitude. This shows that detection via rays directly obstructed by the water layer is difficult in this case, though this is probably not unexpected given the geometry of a shallow water layer deep in the ice. We can actually get a rough idea of the effect of local warmer, shallower ice by examining the left side of Figure 18 for Enceladus above, which shows that the expected count rates for 30 km and 40 km thick ice for *f=0.01* impurity level differ by about 10%, which should be detectable within a year even if a spacecraft spent only part of its time over each latitude. In Phase 2, we will improve our ice model as described above to directly take into account warmer ice over oceans to verify that the reduced attenuation length at ocean latitudes will be detectable.

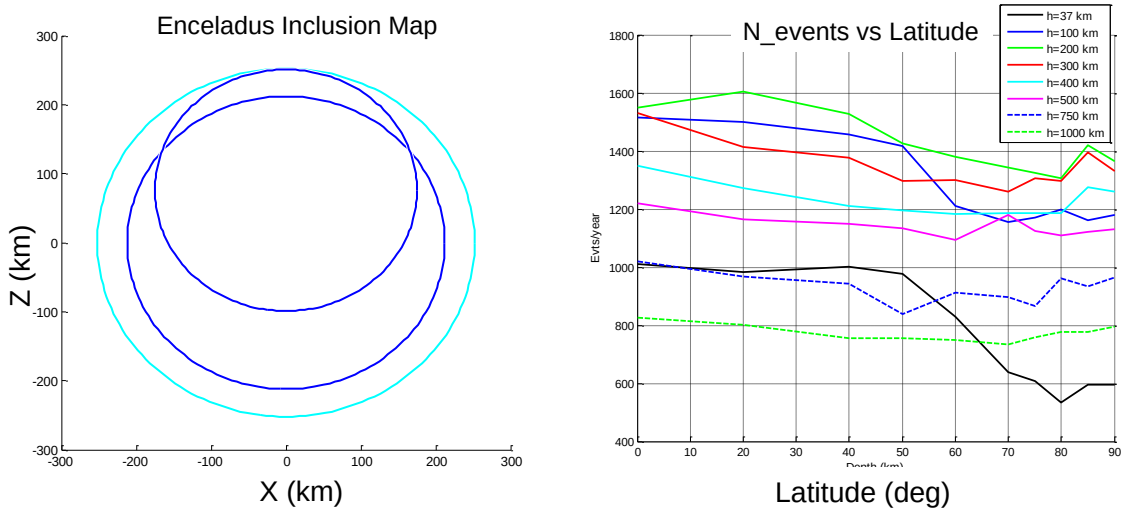

212

Figure 20: Example broad Enceladus inclusion and event rates vs latitude for various satellite altitudes. Left: illustration of inclusion. The light blue line is the ice surface, the larger dark blue circle is the bottom of the ice layer, and the smaller dark blue circle is the outline of the inclusion, modeled as a simple sphere. A small fraction of the top of the sphere intrudes into the ice layer, blocking RF ray paths over a wide but shallow region. Right: Event rate vs latitude of spacecraft.

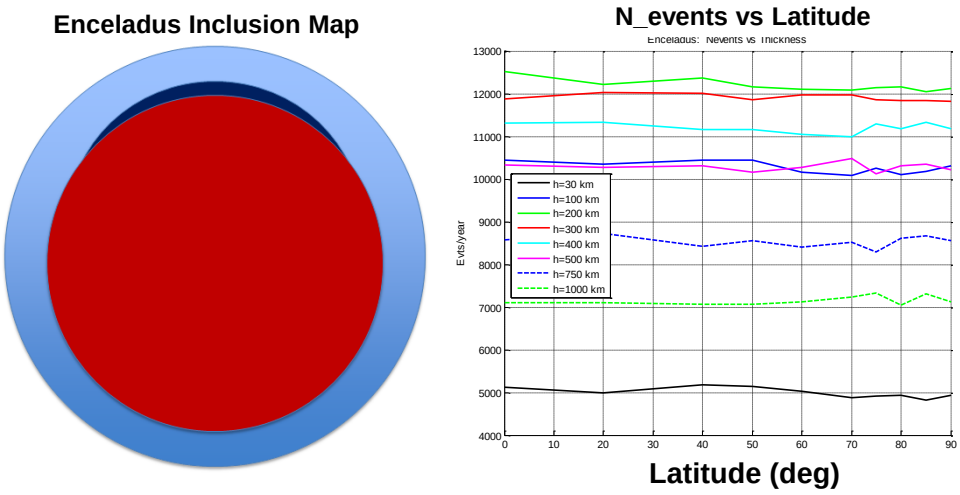

111

Figure 21: Example broad Enceladus inclusion, very deep below the ice surface, and event rates vs latitude for various satellite altitudes. Left: illustration of inclusion. Right: Event rate vs latitude of spacecraft.

We also examined both local and broad ice inclusions for the case of Europa. The geometry for Europa is very different because of its much larger size and much smaller ice depth to moon radius ratio. This has the effect of making local inclusions (those comparable in radius to the ice sheet thickness and thereby much smaller relative to the size of the moon) much harder to detect from latitude-dependent count rates. This is illustrated in Figure 22, which shows a local Europan inclusion of radius 40 km in a 40 km thick ice sheet. The top of the inclusion is 1 km below the top of the ice sheet. The graph on the right side shows that there is no detectable count rate difference vs latitude. As can be seen in the illustration, this is a very small inclusion on the scale of Europa, so detecting features this small could be challenging on large moons. We will investigate this in more detail in Phase 2. Figure 23 shows a case for a broad inclusion on Europa, modeled as a 500 km radius sphere, the top 29 km of which protrudes above the global underice ocean to within 1 km of the ice surface, making a broad region of thinner ice. This inclusion is detectable at altitudes up to 200 km using our current ray-track-only method. We found such inclusions to be detectable at depths up to 5 km on Europa.

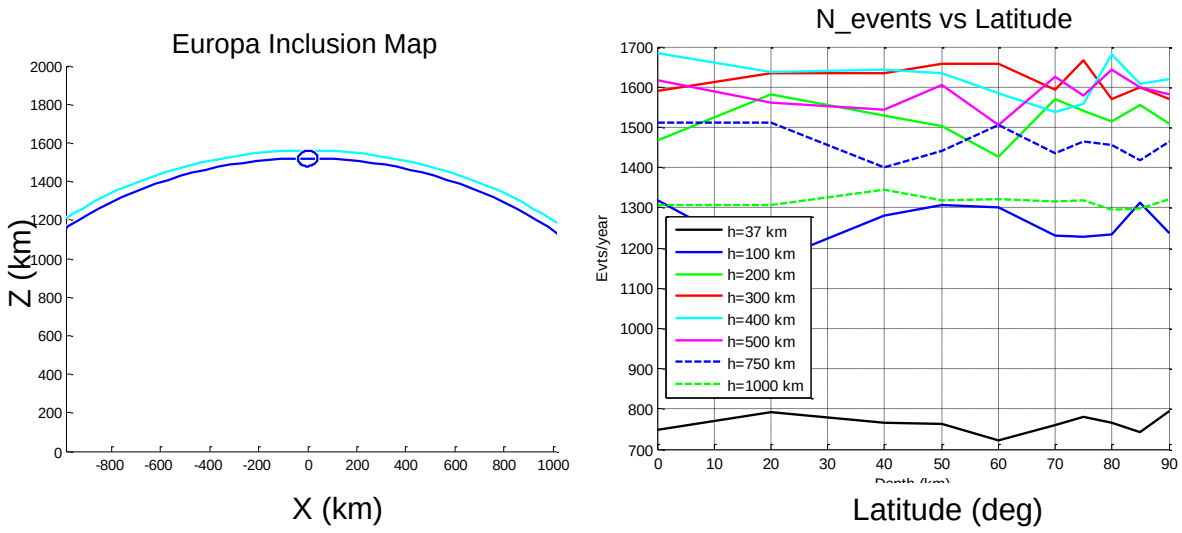

239

Figure 22: Example local Europa inclusion and event rates vs latitude for various satellite altitudes. Left: illustration of inclusion. Right: Event rate vs latitude of spacecraft.

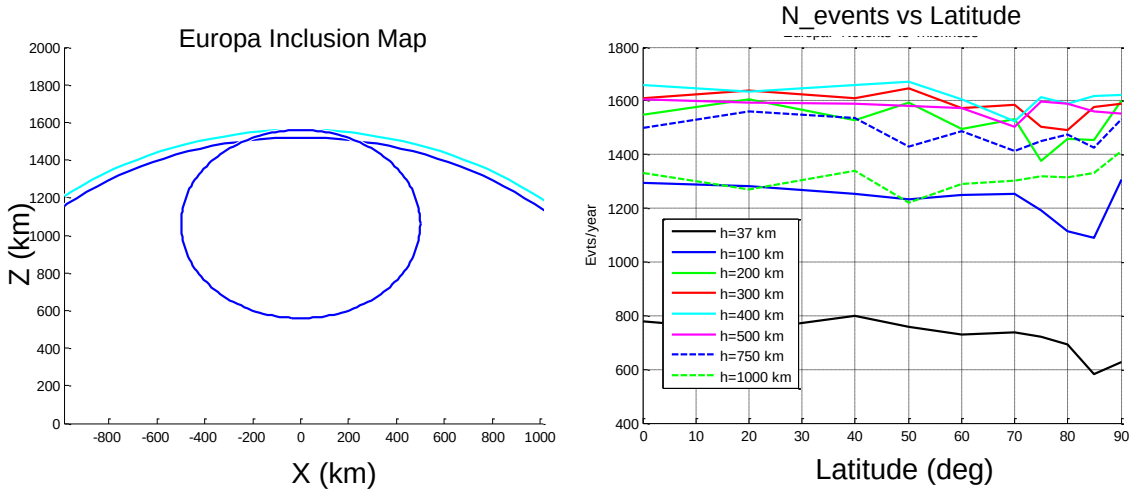

228

Figure 23: Example broad Europa inclusion and event rates vs latitude for various satellite altitudes. Left: illustration of inclusion. Right: Event rate vs latitude of spacecraft.

5.9 ADDITIONAL MEASURABLE QUANTITIES RELATED TO ICE SHEET THICKNESS

We analyzed several new measurable quantities to determine their sensitivity to ice depth, independent of overall event rate. These quantities included event size, zenith angle to surface exit point and cascade location in the ice, and frequency content vs depth. We found promising results for some measurable quantities.

5.9.1 Event Amplitude

Shoji et al [14] found slight indications that event amplitude distribution was indicative of ice sheet depth. We also earlier found hints of this in [9], but with very low statistical significance. Tests of event amplitude distribution for a nominal satellite altitude of 300 km are shown in Figure 24. On the left is a set of normalized histograms of the numbers of events having a given field amplitude for various ice sheet thicknesses. There is some indication that as the ice sheet thickness increases, the relative number of small events near threshold increases and the relative number of larger amplitude events decreases, as expected given the typically larger allowable through-ice path lengths. This is further investigated in the graph on the right, which shows the ratio of the number of events in the smallest amplitude bin to the number in the highest amplitude bin, as a function of ice sheet thickness, for various satellite altitudes. For altitudes above 100 km there is some indication that this ratio increases with increasing ice sheet thickness, but the statistics are poor for one year of simulated data, so the effect is not large. This measureable is considered inconclusive, and will be further investigated in Phase 2, in particular to determine whether it can be combined with other measureable quantities on an event-by-event basis to make a combined measure of cascade depth.

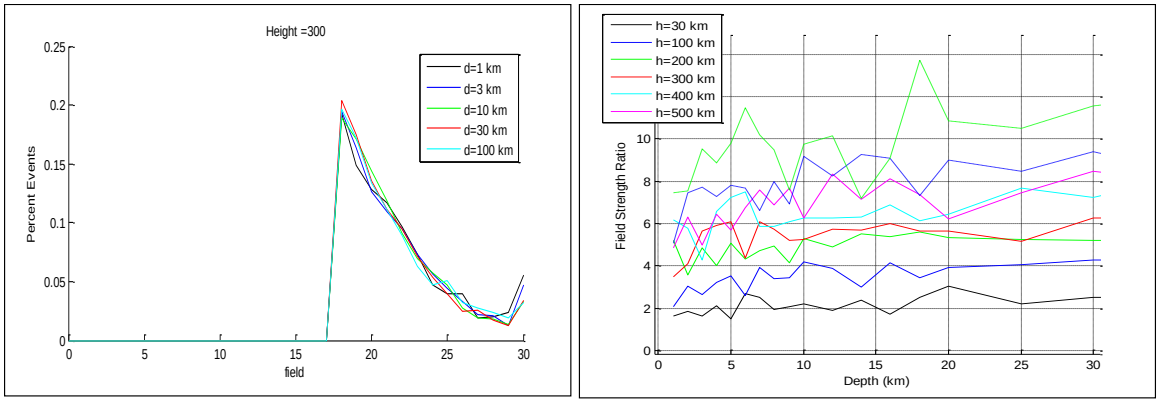

Figure 24: Left: Event size distribution for several Europan ice sheet thicknesses (satellite height = 300 km). As thickness increases, there are relatively more events in the smallest size bin, and fewer in the largest size bin, but the effect is small. Right: Ratio of number of events in the smallest bin to events in the largest bin, vs ice sheet thickness. For satellite altitudes above 200 km there appears to be an increase, but the effect is still small.

5.9.2 Zenith angle to surface exit point and cascade location in the ice

As described earlier, we expect that deeper ice sheets could exhibit different zenith angle distributions due to events occurring over a greater range of zenith angles relative to the observer. Normalized histograms of the zenith angle to both the exit point and interaction point are shown in Figure 25 for a nominal satellite altitude of 300 km. As can be seen, the distributions look very similar for all ice sheet depths, for both the exit point and interaction point. The detection geometry apparently produces events of closely matching zenith angle distribution for all ice depths, even though events can originate deeper for thicker ice sheets, so this measureable unfortunately does not appear very promising so far. This is somewhat surprising in the case of the zenith angle to the cascade, however. Again, we will investigate this further in Phase 2 as an observable to combine with others on single events to attempt to determine possible event depths.

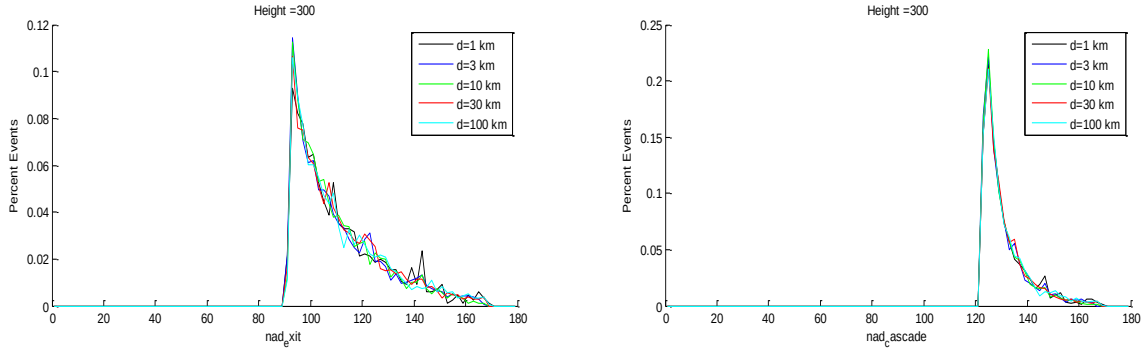

Figure 25: Left: Normalized zenith angle distribution to exit points on surface for detected events, for several ice sheet thicknesses (1 to 100 km). Right: zenith angle distribution to cascade point for several ice sheet thicknesses.

5.9.3 Signal Frequency Content

We simulated the power in three separate adjacent frequency channels at 0.3, 0.6, and 0.9 GHz. One measure of the relative amounts of power in each channel is the ratio of the power in the lowest frequency channel (channel one, 0.3 GHz) to the power in the highest frequency channel (channel three, 0.9 GHz). As depth increases, the scatter plot in Figure 26 shows that this ratio becomes more nearly constant, and that its minimum increases, which would imply more power at lower frequencies, where attenuation is lower. Unfortunately, there is significant variation in individual events, especially from shallow depths, possibly due to variations in how

vertical each path is. The graph on the right shows the probability distribution of events integrated over all detected events for various ice sheet thicknesses. As the ice sheet becomes thicker, the fraction of events in the lowest ratio bin becomes lower due to the deeper events having a higher low frequency to high frequency band power ratio. This appears to be a promising measureable quantity to indicate ice sheet thickness, and will be explored in more detail in Phase 2.

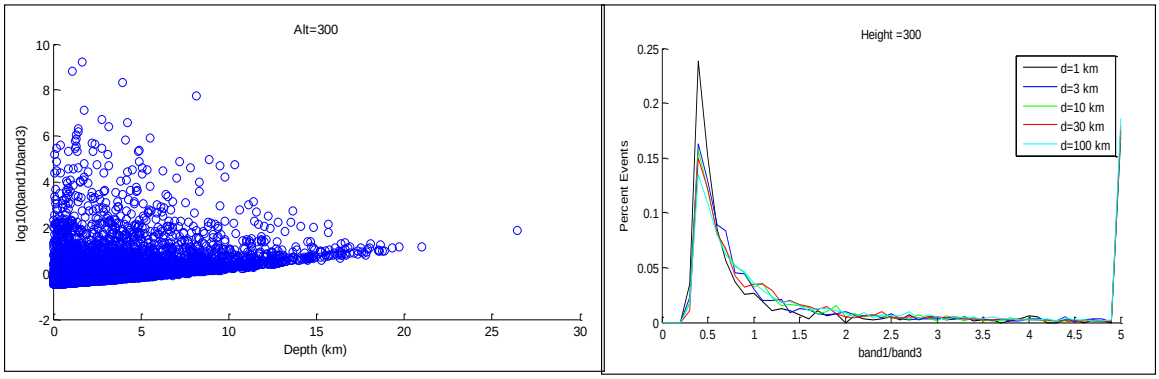

Figure 26: Left: Band 1 to Band 3 intensity ratio vs depth for 30 km thickness. Right: Band 1 to Band 3 intensity ratio distribution for various thicknesses. Percentage in lowest bin decreases as thickness increase.

5.10 COSMIC RAY BACKGROUNDS

Events due to cosmic ray nucleons appear to be a major background source for current Antarctic balloon neutrino pulse detection experiments [8]. The main difference for PRIDE is that there is no thick atmosphere in which the nucleonic cosmic rays might interact, and they hit the surface of the ice directly, causing a surface shower. Detection rates for cosmic ray events and neutrino events are shown in Figure 27. The first thing to note is that the number of cosmic rate events is independent of ice sheet thickness, as it should be. Second, while the number of cosmic ray events is greater than the number of neutrino events, it is not enough to swamp the neutrino signal. For example, at 2 km thickness the yearly neutrino signal of 1500 +- 40 events becomes 1500 + 5000 = 6500 +- 80. At 10 km thickness the neutrino signal of 3000 +- 55 becomes 3000 + 5000 = 8000 +- 90, so 2 and 10 km thicknesses are still more than 10 sigma apart in terms of total number of events detected. Note that, although EeV neutrinos have yet-to-be-discovered, the flux of cosmic ray nucleons has now been fairly well-measured by terrestrial experiments, so the magnitude of this background is, in principle, calculable a priori.

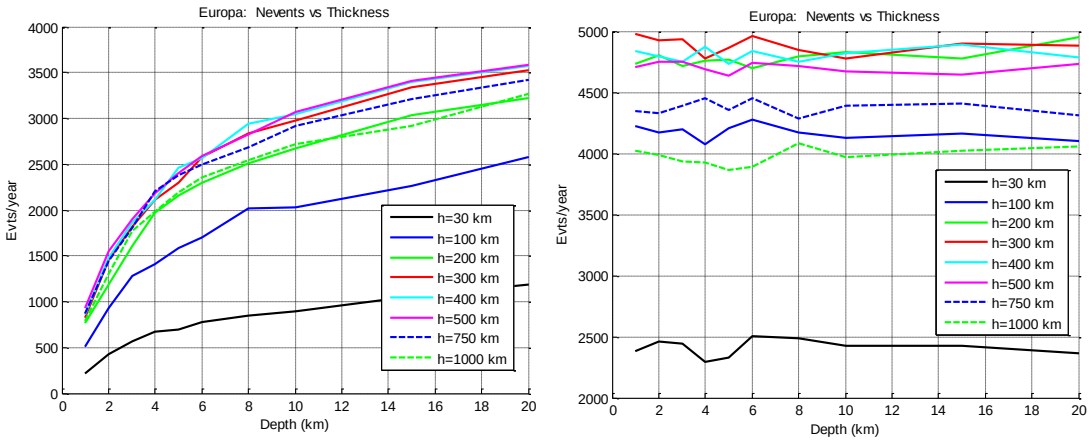

Figure 27: Event rates for Europa for a range of orbit altitudes. Left: neutrinos. Right: nucleonic cosmic rays.

A further examination of cosmic ray vs neutrino events is shown in Figure 28, in which the measured zenith angle of each event is plotted against frequency band amplitude ratio. As discussed earlier, we expect both of these quantities to have different distributions for neutrino and cosmic ray events, so we expect them to fall in different locations on this plot. Neutrino events are shown by green x's, while cosmic ray events are shown by red o's. As can be seen, while there is considerable overlap at low zenith angle (toward the horizon) and smaller ratio (near surface events), there is a large region that can be easily identified as one type of event or the other, implying that additional discrimination of cosmic rays on individual events may be possible. This is a very promising development, and we will continue to explore this issue in more detail in Phase 2 in order to better understand the source of this separation and determine other potential measures that could help us discriminate cosmic ray events from neutrino events with additional efficiency.

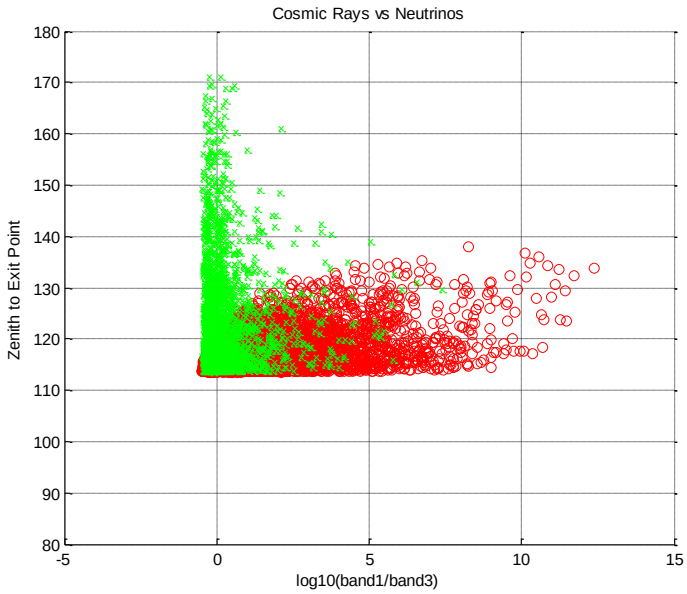

Figure 28: Zenith angle versus the ratio of detector frequency bands for neutrinos (green x's) and nucleonic cosmic rays (red o's). The combined information can be used to discriminate the two signals.

5.11 HARDWARE RESEARCH AND DEVELOPMENT

5.11.1 Digitization and Data Acquisition

Another notable challenge is fast sampling and digitization. As discussed earlier, the Askaryan signal is a short bipolar burst only a few ns in duration, requiring sampling rates of ~1-3 GHz to capture and reliably identify, as shown in Figure 3. Commercial fast ADC's capable of these rates require on the order of 10 W/channel, which is not feasible for an Outer Planet mission. A potential solution is Switched Capacitor Arrays (SCA's), described in [2, 43, 44], which have been used on other high energy physics and cosmic ray physics experiments, such as ANITA, with similar sampling and power requirements. SCA's enable considerable power savings, with each channel requiring only tens of mW [46A]. SCA's have a slow readout, but this does not cause noticeable dead time because the event and random trigger rates should be very low. New generations of SCA's [46] also include onboard triggering, sampling continuously and observing the input signal in real time until the on-chip trigger is generated and accepted, at which point the contents of the SCA is read out. Triggering schemes include options to require both a high and low threshold on each channel, restricted in time ("windowed") to match the bandwidth of the sought-after signal, which has been proven to considerably reduce false alarms and hence allow an increase in sensitivity by reducing SNR threshold requirements, as Askaryan RF pulses are brief and strongly bipolar, while thermal fluctuations will be random in nature.

We leveraged existing efforts on developing low power digitizer technology to develop a chip applicable to PRIDE with 2 Gs/s rate, 1.5 GHz bandwidth, and expected favorable radiation hardness properties, and which uses only 32 mW per channel, ideal for a deep space mission. Figure 29 shows a plot of the new SCA layout, dubbed "SST" for Synchronous Sampling plus Trigger. Less than one-third of the rather small (~2.5 by 2.5mm) chip includes the active sampling and trigger circuitry. For high performance, a small 58-pin, 8 mm surface mount package was employed. The SST was designed for simplicity of operation, and only three active controls are required for operation: a Start/Stop pin that starts and stops sampling, a Reset pin, and a Read Clock pin. The packaged design, in fine-pitch 8mm packaging, is shown in Fig. 30.

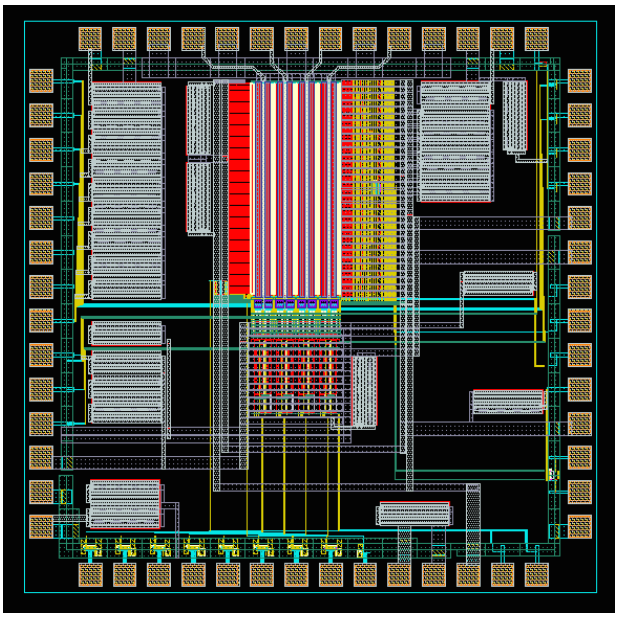

Fig. 29: A plot of the SST. The dimensions are approximately 2.5 by 2.5mm.

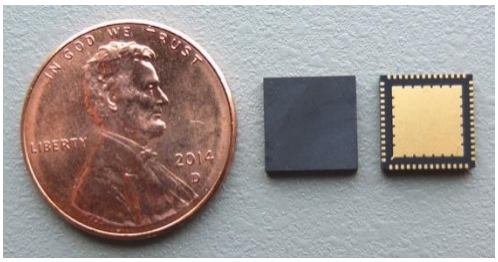

Fig. 30: SST device in 8 mm packaging (top and underside shown separately).

The SST's high speed sampling clocks are generated by a fast shift register containing a single "1" as a pointer. As shown in Fig. 31, the base input clock is provided via an LVDS

receiver followed by a 2-phase clock generator, which feeds a buffer tree that distributes the clock in a highly-uniform fashion to the shift register. The shift register is dynamic and consists of 128 master-slave flip-flops configured in a circular fashion. Both the master and slave sections of the flip-flops are used to generate sample clocks, and hence the sample rate is doubled by interleaving, e.g. a 1 GHz clock results in a 2 G-sample/s rate. Being formed exclusively by clocked digital logic, the sampling rate range is 6 orders of magnitude wide (≤2 kHz to ≥2 GHz). Its timing uniformity remains consistent regardless of its clock speed, based mostly on that of the LVDS clock source, for which ≤1ps jitter is commonly achieved.

In many applications, including PRIDE, the SST would be operated in a common-stop mode, endlessly sampling until it is stopped by a trigger, at which time the preceding samples contain the signal of interest. The position of the stop may hence be random relative to the start, yet knowing its position remains important in order to delineate the beginning and end of the record. Therefore, the position of the pointer at the moment it is stopped is read out in parallel with the analog samples. Unlike many PLL-based schemes, the SST can be started and stopped instantly, and common-start operation is equally easy.

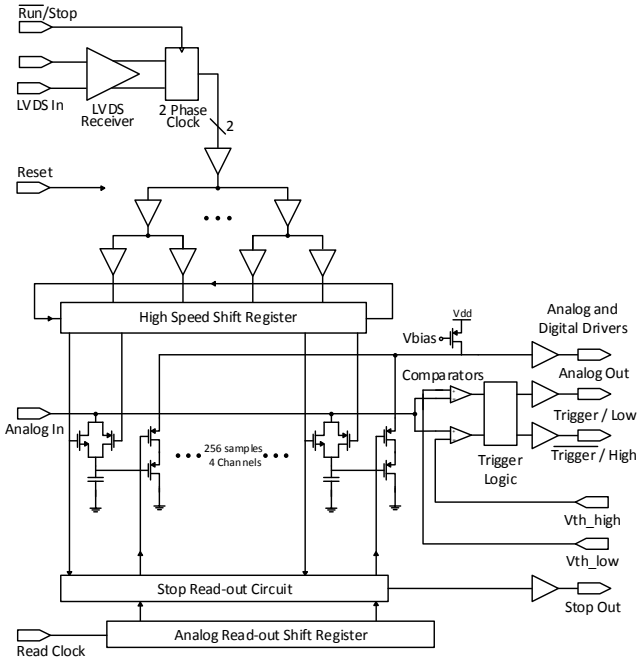

Fig. 31: Device overview showing clock features and one channel of four.

The SST incorporates high-performance real-time trigger circuitry, depicted in Fig. 32. Each channel includes two fast comparators, intended for High and Low thresholds. Each pair of comparators observes its channel's analog input directly, with no gain, buffering or level-shifting before-hand. With direct, individual control over comparator inputs, setting thresholds is an easy process. For both high-speed and high gain, the comparators use a large number of fast (~1.2 GHz bandwidth) but low-gain (~3.3 V/V) stages. The comparators can thus discriminate voltage

differences with (conservatively) over 600 MHz bandwidth, e.g. small pulses with 500 ps full-width at half-maximum are discriminated, and achieving a voltage sensitivity of 1 mV, RMS.

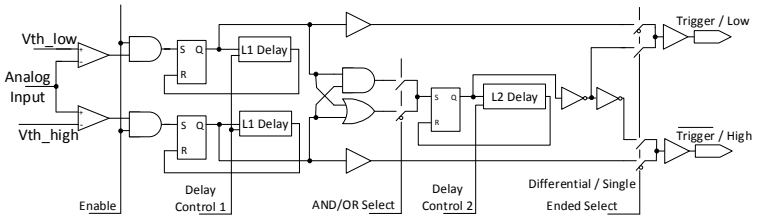

Fig. 32: Trigger logic including enable, pulse-stretching latches and delay lines, AND/OR selection and AND/OR pulse-stretching, and selection of dual single-ended or differential outputs.

Fig. 33 shows a portion of a test board that was used for a majority of the results presented here. There are 4 analog inputs at the left, via SMA edge connectors, the SST in the center, and an FPGA that handles the SST's trigger outputs and controls the SST's readout, manages the setting of thresholds via an 8-channel DAC, and buffers the digitized data (from 12-bit ADC's). Bias-tee circuits are used between the SMA analog inputs and the SST inputs in order to provide an AC-coupled arbitrary voltage offset at the SST. Termination of the analog inputs is by AC-coupled 50 Ohm resistors in order to reduce DC power consumption of the termination while using an input offset. A 1 GHz LVDS oscillator is used to clock the SST. The rest of the board includes a microcontroller, power control and conditioning including switching DC-DC converters, solid-state relays, linear regulators, and various other components. Thus, all measurements reported here include the noise and other typical non-ideal effects of a realistic system, the quantization noise from 12-bit analog to digital conversion, etc.

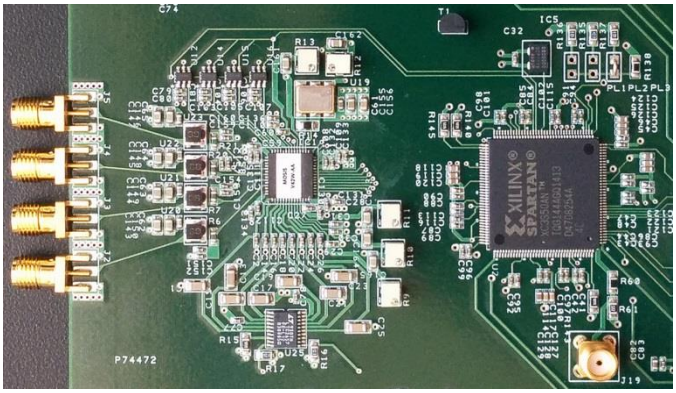

Fig. 33: Test board close-up showing 4 analog inputs (left edge, via SMA connectors), bias-tee circuits to provide AC-coupled analog signal offsets, the 2 GHz SST chip (center), and an

FPGA (right) for managing triggers and event readout, etc. A temperature monitor is seen at the upper edge of the photograph.

Fig. 34 shows an example acquired waveform, that of a 100 MHz sine wave, after basic fixed-pattern noise ("pedestal") subtraction.

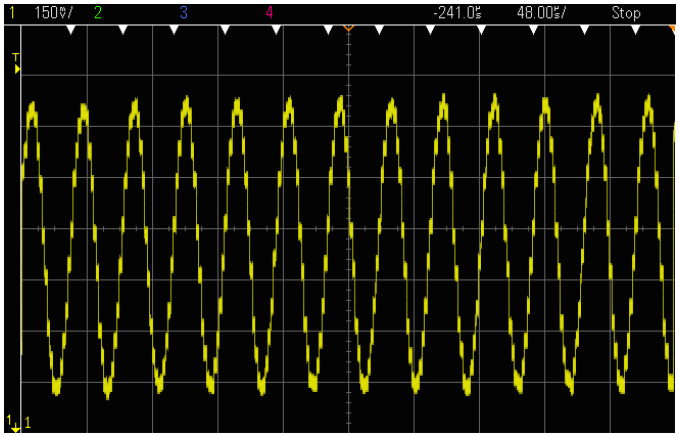

Fig. 34: SST digitized readout of a 100 MHz sine wave sampled at 2 GHz.

The resulting sampling noise, bandwidth, linearity, fixed pattern noise and leakage rate were excellent. Sampling noise of ~0.42 mV was measured, resulting in a dynamic range of 12 bits. The bandwidth was measured by applying sine waves of fixed amplitude but varying frequency from a signal generator with a standard 50 Ohm output impedance (Agilent N5181AEP-002). Bias-tee circuits were employed that provided a DC offset at the SST's inputs of 0.9V, the middle of the SST's range so as to optimize for bipolar signals. The SST recorded these sine waves at 2 G-samples/s, and the sampled analog output of the recorded sine waves were observed and normalized to unity gain at low frequencies. As seen in Fig. 35, the resulting bandwidth was flat to about ±0.5 dB out to 1.3 GHz, and the -3 dB bandwidth was found to be slightly over 1.5 GHz.

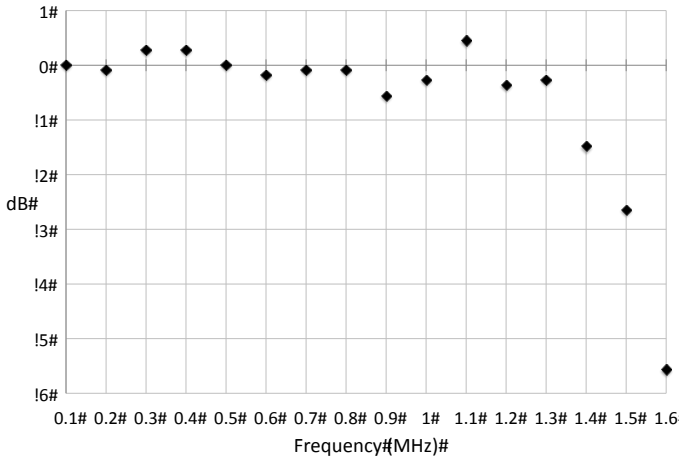

Figure 35: Gain (magnitude) vs. frequency of the SST, normalized to 0 dB. The -3 dB point is just over 1.5 GHz.

For PRIDE, the essential ability to respond to Askaryan-effect pulses leads to a few figures of merit: The SST should respond to pulses of 0.5-1.5 ns, full-width at half-maximum (FWHM), and an amplitude of one sigma or smaller than ARIANNA's thermal noise level, namely under about 17 mV using its current amplifier design. Figure 36 shows one such pulse and resulting trigger. The bottom trace shows a pulse that is ~15 mV high (~7.5 mV at FWHM) and ~500 ps wide at FWHM (trace gain is 5 mV/division, horizontal time-base is 2 ns/division), and hence is below ARIANNA's specification in amplitude. This was the fastest pulse that our laboratory's equipment permitted and would translate, conservatively, to a comparator bandwidth of at least 600 MHz (possibly up to 1 GHz). The upper trace shows the trigger output for that comparator. This trace has a gain of 1V/division, 200 times greater than that of the input pulse trace. The output logic level is set at 2.5V. Note that the delay between the input pulse and the comparator output pulse is dominated by cable and probe delays, and is actually about 2.6 ns. The SST successfully discriminates a pulse of this nature 100% of the time. Furthermore, the voltage difference of such pulses required to cause 0% triggers and 100% triggers was found to be no more than 4 mV, and hence its voltage sensitivity has an estimated sigma of ~1 mV or less.

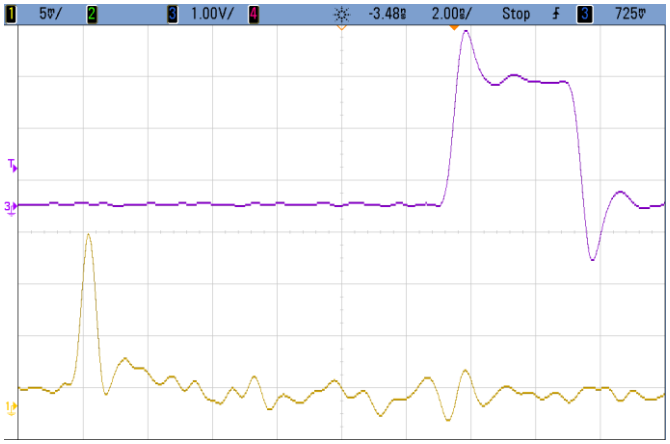

Fig. 36: Trigger output (top trace) in response to a ~15 mV input pulse of ~0.5ns full-width at half maximum (lower trace). Note that the vertical scale is 200 times larger for the top trace (signal output) vs. the lower input signal, which is 5 mV/division.

To summarize, a fully synchronous analog transient waveform recording and triggering I.C., the "SST," containing 4 channels of 256 cells per channel with on-chip trigger circuitry is appropriate for the PRIDE application. It was fabricated in a 0.25µm, 2.5V process to preserve a wide input range (0-1.9V), low kT/C noise (~0.23 mV RMS at room temperature) and low signal leakage (~150 mV/s) for high dynamic range (>11.5 bits). Its maximum specified sample rate is 2.5 GHz. Optimized design and packaging yielded a nearly flat analog bandwidth to ~1.3 GHz using a standard 50-Ohm signal source, and a -3 dB bandwidth of ~1.5 GHz. Power consumption is under 140 mW for four channels with maximum comparator and LVDS power. The SST includes a dual-threshold coincidence trigger per channel that operates with ~1 mV RMS resolution with at least 600 MHz bandwidth.

A two-level trigger can be implemented for suppression of backgrounds. The first level consists of two comparators (generally with High and Low thresholds) whose outputs are digitally stretched to allow a coincidence between them to be formed over a specified time. An AND or an OR can be formed between these two stretched comparator results. This is then stretched again to allow coincidences between channels to be formed; the result is then presented on differential outputs. Alternatively, the individual stretched comparator results can be presented on the same trigger outputs, but in single-ended form. To help further suppress cross-talk between the trigger outputs and the analog inputs, the trigger output pins automatically adapt to lower voltages, e.g. positive ECL (0.8V) or 1.2V CMOS.

Particular effort during the NIAC Phase I program was made in understanding the details of the SST's timing accuracy. A timing accuracy of ~5 ps was obtained for triggered signals, with an ultimate timing accuracy of under ~1.5 ps already achieved . These values are among the best achieved by such devices and are fully compatible with the needs of the PRIDE application. A summary of the SST's specifications and performance is given in Table 8.

Table 8: SST Figures of Merit

Parameter	Value
Technology:	0.25 μm CMOS
Supply voltage:	2.5V
Number of channels:	4
Samples per channel:	256
Chip size:	2.5 by 2.5 mm
Package size:	8 mm by 8 mm
Number of package pins:	56
Input clock (typical):	1 GHz LVDS
Sample rate (typical):	2 GHz
Minimum sample rate:	< 2 kHz
Analog bandwidth:	> 1.5 GHz, -3dB
Power per channel with trigger:	32 mW at 2 GHz
Analog input range:	0-1.9V
Input referred temporal noise:	0.42 mV
Dynamic range:	12 bits, RMS
Fixed pattern noise:	~ 6.5 mV, RMS
Integral non-linearity (0.1-1.7V):	0.6% over 1.6 V
Integral non-linearity (0.4-1.4V):	0.3% over 1V
Crosstalk from 1.6V sine wave:	<1% at 300 MHz
Leakage rate:	0.15 V/s
Trigger comparators per channel:	2 (High and Low)
Trigger sensitivity:	< 1 mV, RMS
Trigger bandwidth:	> 600 MHz
Trigger functions per channel:	AND/OR, windowed
Trigger output modalities:	Differential/Individual
Trigger output voltage:	0.8, 1.2 or 2.5V CMOS
Trigger time walk:	360 ps
Uncorrected timing FPN:	30.4 ps, RMS
Timing resolution after calibration:	≤ 1.46 ps, RMS
Resolution minus oscillator jitter:	0.86 ps RMS (est.)

5.11.2 Receiver Design

As discussed earlier, another major risk is that the antennas required will be too large, or too many, to fit within spacecraft mass and size requirements. We did not perform any quantitative antenna research or development in Phase 1, but we have considered the issues

involved in order to develop a detailed plan for several antenna-related development activities in Phase 2. We will undertake an effort to first identify a workable receiver design and then to model a prototype in order to demonstrate mass, size, and performance requirements.

Interference suppression may be achieved by the inherent pattern of the receiving antenna when the interfering signal comes from a different direction than the target. In Miller et al [9] we considered a straw-man antenna design based upon a commercial starting point, modified for the PRIDE application. The wide bandwidth used in the simulated signal calculation could be achieved with a ridged horn antenna. We confined the beam in the elevation plane to around 20° about the horizon by employing a quad-ridge antenna with dimensions that were 35 cm deep by 72 cm in the elevation plane by 8 cm in the azimuth plane. Its estimated mass is 1-2 kg, which met all the then known requirements. However, our Phase 1 study reveals that the quad-ridge solution has its highest gain at high frequencies that are more severely attenuated by the ice than lower frequencies where the Askaryan signature has greater detectable energy (see Figure 10). Thus we need to explore other approaches such as a log-periodic dipole array (LPDA) being considered for ARIANNA or a sinuous antenna whose characteristics can be tailored to better match the spectral characteristics of the received signal. However, LPDA and sinuous antennas have poorer pattern discrimination than the quad-ridge horn owing to their intrinsically larger group delay across the bandpass. Nevertheless, as described in the digitizer section, considerable discrimination can be achieved at the digitization and triggering stage, as well. A primary goal of Phase 2 will be development of simulations including detailed antenna, digitizer and trigger properties and trade studies to arrive at an optimum system design to provide both background rejection and depth measurement.

Polarization discrimination offers another approach for suppression of interference. This method relies on the difference in polarization properties of the Askaryan pulse relative to interference such as burst RF emissions that emanate from Jupiter. The polarization state of each signal is determined by real elements S_0, S_1, S_2, and S_3 of the Stoke's vector, in terms of which the degree of polarization, d_P, is determined by

$$d_P = \frac{\sqrt{S_1^2 + S_2^2 + S_3^2}}{S_0}$$

Burst RF emissions from Jupiter are likely to be randomly polarized for which $d_P \approx 0$, whereas Askaryan signals are known to have pronounced polarization characteristics. Thus, a dual-polarization receiver architecture in conjunction with Stoke's processing on board can provide interference rejection. Unlike pattern suppression, polarization discrimination operates independent of co-alignment of desired and interfering sources. However, this approach requires two gain- and phase-balanced receiver channels per antenna; either horizontal and vertical or right-circular and left-circular polarizations to implement a Stokes receiver. In this regard, the sinuous antenna provides a more compact implementation than the LPDA. The quad-ridge horn also offers dual polarization but with a mismatched spectral response as mentioned previously. Any attempt to spectrally match the gain of the quad-ridge horn to that of the received Askaryan signal results in a large (2.9 m in elevation, 1.5 m deep) structure that prohibitively taxes mass and volume requirements.

Spectral differentiation provides yet another method of eliminating interference from desired signals. In this case, each captured signal is matched against a spectral template and retained or discarded in accordance with some criterion based on degree of correlation. The greater attenuation of high frequency spectral components of the Askaryan signal by the ice reduces the effectiveness of this approach, and we anticipate its use in conjunction with pattern and/or polarization discrimination.

Trade studies are required for the next level of design to determine event rate and reconstructed angular distribution for antenna designs of varying bandwidth, and acceptance, in order to determine more detailed receiver requirements to meet the top level requirement of deep ice depth measurement capability. Construction and testing of a prototype will then be necessary to demonstrate sensitivity, bandwidth, and acceptance, which we expect to be a major part of any post-NIAC effort.

5.12 MISSION CONCEPTS

The original concept of this instrument was as a complement to the IPR on a Flagship mission to the outer planets [13A]. However, the properties of the signal we are trying to detect are similar to those of the IPR. Since the IPR uses a considerable amount of spacecraft power, it could be used over particular regions of interest, while the rest of the time, PRIDE could be collecting data in passive mode. Finally, a new concept for PRIDE deployment beyond the scope of our Phase 1 study is Cubesats. A multi-satellite version of PRIDE would have the tremendous advantage of being able to triangulate received signal directions to pinpoint the 3D location of the original cascade within the ice, thus directly measuring the depth of any events detected by multiple satellites. This approach had seemed beyond the scope of a low cost concept like PRIDE, but this may have changed recently with the development of interplanetary cubesat concepts [45]. Due to the low power and small size requirements of individual antenna/receiver channels, our receivers may be suited to deployment on multiple Cubesats. We could, for example, fold up a 600 MHz tripole into a 3U Cubesat. This will be investigated quantitatively in Phase 2. We are just beginning to explore these concepts and will make them part of our Phase 2 Antenna and Mission Concept Studies.

6. CONCLUSIONS

The purpose of the PRIDE instrument is to measure the thickness and gross distribution of ice sheets covering icy moons using a new passive low-cost, low-power, low-mass instrument. Such an instrument could benefit, and also fit onto any future Jovian or Saturnian missions, potentially making this measurement at SWaP savings and thereby freeing resources that could enable additional science goals. Our goal in Phase 1 was to show promise and benefit of the concept in more realistic conditions. We made considerable progress in several areas, including:

- Implementation of realistic ice models and identification of models for which significant ice sheet depth measurement capabilities exist.

- Adaptation of three existing, independent, higher fidelity detector simulations used in the EHE astrophysics community to the PRIDE application, and comparison of results to verify expected event rates.
- Implementation of models for other ice moons: Ganymede, Callisto, and Enceladus, and for both Polar and Equatorial ice profiles.
- Implementation of an initial model of local water inclusions within ice sheets.
- Analysis of new measurable quantities to determine their ability to determine ice depth independently of overall event rate.
- Leveraging of existing efforts on low power digitizer technology development to develop a chip applicable to PRIDE with 2 Gs/s rate, 1.5 GHz bandwidth, and expected favorable radiation hardness properties, which uses only 32 mW per channel, ideal for a deep space mission.
- Initial analysis of cosmic ray events, which are expected to be a major background for PRIDE.
- Establishment of an MOU with Russian EHE neutrino researchers at the Lebedev Physical Institute.

Our Phase 1 Study has made significant progress in demonstrating both feasibility and benefit. Our primary conclusion is that the PRIDE concept shows considerable promise under more realistic conditions, and we have developed a detailed Phase 2 study plan and proposal to further advance the concept.

7. FUTURE PLANS

In Phase II we will further reduce risk, explore capability, and arrive at a detailed baseline mission concept. The effort will focus on reducing the remaining risk areas we could not explore fully in Phase 1 and advancing the TRL of the concept via (a) simulation development for analysis of depth measurement capability and (b) hardware development. A brief overview of our Phase 2 study plan follows, and details can be found in our Phase 2 Proposal. The final products will be a white paper detailing the reduction of the described risks, and a proposed baseline instrument and mission design.

Remaining Risk Reduction

- We will develop a more complete mission simulation based upon ice attenuation length vs 3D location in the entire ice shell, which will allow us to study detailed design issues:
    1. More detailed analysis of background from nucleonic cosmic rays and Jovian RF noise sources.
    2. Detailed study of local water inclusions, such as are expected on Enceladus
    3. Surface ice roughness effects.
    4. Events in which both a direct signal and a reflected signal from the ice-water interface are detected, which could allow depth measurement with only a few events.
    5. Polarization and birefringence effects.

Detailed design trade studies

- Improved fidelity of our simulations in several areas to allow us to study additional detailed design issues and conduct system-level trade studies to arrive at a baseline instrument and mission design.
- Digitizer chip design aimed at radiation hardness and low power
- We will study specific mission concepts and analyze the utility of PRIDE compared to an IPR in multiple possible mission contexts

Technology Development

- Study vulnerability to outer planet radiation environments
- Detailed antenna and array configuration and response, including triggering approaches, to maximize depth measurement capability and digitizer/trigger background rejection while minimizing SWaP.

Tim C. Miller
Johns Hopkins University
Applied Physics Lab

8. REFERENCES

[1] Waxman, E. and Bahcall, J.N., 1998. High energy neutrinos from astrophysical sources: An upper bound. Phys.Rev. D59, 023002.

[2] Kleinfelder, S. 2003. Advanced transient waveform digitizers, Proc. SPIE 4858, 316-326.
Kleinfelder, S. 2003. A Multi-GHz, Multi-Channel Transient Waveform Digitization Integrated Circuit. IEEE Transactions on Nuclear Science 50, 955 – 962.

[3] Structure and Evolution of the Universe Roadmap: Beyond Einstein, from the Big Bang to Black Holes, 2003, http://science1.nasa.gov/media/medialibrary/2010/03/31/Beyond-Einstein_.pdf.

[4] Gorham, P. W., 41 colleagues, 2009. The Antarctic Impulsive Transient Antenna Ultra-high Energy Neutrino Detector: Design, Performance, and Sensitivity for the 2006–2007 balloon flight. Astropart. Phys. 32,10.

[5] Allison, P., et al., 2012, Design and Initial Performance of the Askaryan Radio Array Prototype EeV Neutrino Detector at the South Pole, Atroparticle Phys., **35**, 457.

[6] Gerhardt, L., Klein ' S., Stezelberger, T., Barwick, S., Dookayka, K., Hanson, J., Nichol, R. 2010, A prototype station for ARIANNA: A detector for cosmic neutrinos, Nucl. Inst. Meth. A, **624**, 85.

[7] Kravchenko, I., 20 colleagues 2006. RICE Limits on the Diffuse Ultrahigh Energy Neutrino Flux. Phys. Rev. D73, 082002, 1-19.

[8] Hoover, S., 44 colleagues, 2010. Observation of Ultra-high-energy Cosmic Rays with the ANITA Balloon-borne Radio Interferometer. arXiv: 1005.0035v2 [astro-ph.HE] 12 May 2010.

[9] Miller, T.C., Schaefer, R., Sequeira, H.R., 2012. PRIDE (Passive Radio [frequency] Ice Depth Experiment): An Instrument to Passively Measure Ice Depth from a Europan Orbiter using Neutrinos, 2012, Icarus, 220, 877-888.

[10] Connolly, A., 2013, ICEMC ANITA and ARA Simulation Documentation and Repository, http://www.physics.ohio-state.edu/~connolly/doxygen_icemc/html/index.html, http://www.physics.ohio-state.edu/~connolly/icemc/icemcinstr.html.

[11] Shoji, D.; Kurita, K.; Tanaka, H. K. M., Efficiency of neutrino-induced radio measurements to inspect local areas of Enceladus, 2012, Icarus, **218**, 1, 555-560.

[12] Chyba, C. F., Ostro, S. T., Edwards, B. C. 1998. Radar Detectability of a Subsurface Ocean on Europa. Icarus 134, 292-302.

[13] Schaefer, R. K., Miller, T.C., and Sequeira, H.B. 2009, An Instrument For Measuring Ice Thickness On Europa, Synergistic Science & Instrument Poster Abstracts, Europa Jupiter System Mission Instrument Workshop, July 15-17, 2009. p 38.
Miller, T.C., Schaefer, R., Sequeira, H.R., 2012. PRIDE – Passive Radio Ice Depth Experiment - An Instrument to Measure Outer Planet Lunar Ice Depths from Orbit using Neutrinos, *Fall AGU Meeting*, P23D-04.
T. Miller, R. Schaefer, H.B. Sequeira, and G.W. Patterson, 2013. PRIDE – Passive Radio Ice Depth Experiment - An Instrument to Measure Outer Planet Lunar Ice Depths from Orbit using Neutrinos, TeV Particle Astrophysics (TeVPA), Aug 26-29, 2013, University of California, Irvine, CA.

T. Miller et al, 2014. PRIDE – Passive Radio Ice Depth Experiment - An Instrument to Measure Outer Planet Lunar Ice Depths from Orbit using Neutrinos. Workshop in the Habitability of Ice Worlds, Feb 5-7, 2014, Pasadena, CA.

[14] Shoji, D., Kurita, K., and Tanaka, H.K.M., 2011, Constraint of Europan ice thickness by measuring electromagnetic emissions induced by neutrino interaction, Geophys. Res. Lett., 38, L08202.

[15] Schenk, P. M. (2009), Slope characteristics of Europa: Constraints for landers and radar Sounding, Geophys. Res. Lett., 36, L15204, doi:10.1029/2009GL039062.

[16] Berquin, Y., Kofman, W., Herique, A., Alberti, G., and Peck, B. 2012, A study on Ganymede's surface topography: Perspectives for radar sounding. Planetary and Space Science (2012), http://dx.doi.org/10.1016/j.pss.2012.07.004

[17] Chyba, C. F., Ostro, S. T., Edwards, B. C. 1998. Radar Detectability of a Subsurface Ocean on Europa. Icarus 134, 292-302.

[18] Donald D. Blankenship, Duncan A. Young, William B. Moore, John C. Moore, Radar Sounding of Europa's Subsurface Properties and Processes: The View from Earth.

[19] John C. Moore, Models of Radar Absorption in Europan Ice, Icarus 147, 292–300 (2000).

[20] Stevenson, D.J. et al. (2014-04-04). "The Gravity Field and Interior Structure of Enceladus". Science 344 (6179): 78–80.

[21] **NASA Jupiter Europa Mission Study Final Report**, http://sci.esa.int/ejsm-laplace/48278-jupiter-europa-orbiter-mission-study-2008-final-report/**, 2009.**

[22] Carr, T. D., Desch, M. D., Alexander, J. K. 1983. Phenomenology of magnetospheric radio emissions. In: Dessler, A.J. (Ed), Physics of the Jovian Magnetosphere. Cambridge Univ. Press, New York, pp. 226-284.

[23] Committee on the Planetary Science Decadal Survey, Space Studies Board, Division on Engineering and Physical Sciences, 2011. Vision and Voyages for Planetary, Science in the Decade 2013-2022.

[24] Gorham, P. W. 2004. Planet-sized Detectors for Ultra-high Energy Neutrinos & Cosmic Rays, Proc. NASA Advanced Planning Office's Capability Roadmap Public Workshop, 38.

[25] Matsuoka, T., Fujita, S., Mae, S. 1996. Effect of temperature on dielectric properties of ice in the range 5–39 GHz. Journal of Applied Physics 80, 5884 – 5890.
Mätzler, C. 2006. Microwave dielectric properties of ice. In: Mätzler, C., Rosenkranz, P. W., Battaglia, A., Wigneron, J. P. (Eds.), Thermal Microwave Radiation: Applications for Remote Sensing, Stevenage, pp. 1-8.
Warren, S. G. 1984. Optical constants of ice from the ultraviolet to the microwave. Applied Optics 23, 1206–1225.
Warren, S. G., Brandt, R. E. 2008. Optical constants of ice from the ultraviolet to the microwave: A revised compilation. Journal of Geophysical Research 113, 1-10.

[26] Barwick, S.; Besson, D.; Gorham, P.; Saltzberg, D., 2005. South Polar in situ radio-frequency ice attenuation, Journal of Glaciology, 51, 173, pp. 231-238.

[27] Barwick, S. W., 30 colleagues 2006. Constraints on Cosmic Neutrino Fluxes from the ANITA Experiment. Phys. Rev. Lett., 96, 171101, 1-4.

[28] Gorham, P. W. 40 colleagues 2007. Observations of the Askaryan Effect in Ice. Phys. Rev. Letters 99, 171101, 1-5.

[29] Saltzberg, D., Gorham, P., Walz, D., Field, C., Iverson, R., Odian, A., Resch, G., Schoessow, P., Williams, D. 2001. Observation of the Askaryan Effect: Coherent Microwave Cherenkov Emission from Charge Asymmetry in High Energy Particle Cascades. Phys. Rev. Letters 86, 2802, 2802-2805.

[30] Hand, K. P., Chyba, C. F. 2007. Empirical constraints on the salinity of the europan ocean and implications for a thin ice shell. Icarus 189, 424-438.

[31] Gorham, P.W. et al, 2011, The ExaVolt Antenna: A Large-Aperture, Balloon-embedded Antenna for Ultra-high Energy Particle Detection, Astroparticle Phys., **5**, 242.

[32] [18] Ryabov, V.A., Gusev, G.A., Lomonsov, B.N., Polukhina, N.G., and Chechin, V.A., 2010, Lunar Orbital Radio Detector and Detection of Ultrahigh Energy Particles, Bulletin of the Lebedev Physics Institute, **37**, 98-103.

[33] Lehtinen, N.G., Gorham, P.W., Jacobson, A.R., Roussel-Dupr´e, R.A. 2008. FORTE satellite constraints on ultra-high energy cosmic particle fluxes, arXiv:astro-ph/0309656v2.

[34] Gaisser, T. K. 1990. Cosmic Rays and Particle Physics. Cambridge Univ. Press, New York.

[35] Gaisser, T. K., Stanev, T. 2007. Cosmic Rays, Proc. World Particle Data Group, 1-20.

[36] Griswold, M., Harrison, M., and Saltzberg, D., 2007, Observation of Light Transmission Through Randomly Rough Glass Surfaces Beyond the Critical Angle, J. Opt. Soc. Am. A., 24, 3207.

[37] Daub, B., Everson, E., Griswold, M., Harrison, M., Connolly, A., Saltzberg, D. 2006. Optical Modeling of the Effect of Surface Roughness on Detection of Signals from Within the Ice with ANITA, www.phys.hawaii.edu:8080/anita_notes/060310_140009/roughness_note.pdf.

[38] Dogariu, A., Boreman, G.D., 1996, Facet Model for Photon Flux Transmission Through Rough Dialectic Interfaces, Optics Lett., 21, 701.

[39] Black, G.J., Campbell, D.B., Nicholson, P.D. 2001. Icy Galilean Satellites: Modeling Radar Reflectivities as a Coherent Backscatter Effect, Icarus 151, 167–180.

[40] Campbell, D.B., Chandler, J.F., Ostro, S.J., Pettengill, G.H., Shapiro, I.I., 1978. Galilean Satellites: 1976 Radar Results, Icarus 34, 254-267.

[41] Ostro, S.J., 11 colleagues 1992. Europa, Ganymede, and Callisto, New Radar Results From Arecibo and Goldstone, Journal of Geophysical Research, 97, Ell, 18,227-18,244.

[42] Gusev, G A, Lomonosov, B N, Ryabov, V A , Chechin, V A , Physics ± Uspekhi 53 (9) 915 ± 921 (2010).

[43] Varner, G. 2003. Self-Triggered Recorder for Analog Waveforms v. 3 (STRAW3) Data Sheet, Dept. Of Physics, University of Hawaii.

[44] Varner, G. 2004. Large Analog Bandwidth Recorder and Digitizer with Ordered Readout (LABRADOR) User's Manual, Dept. Of Physics, University of Hawaii.

[45] Staehle, R.L, et al, "Interplanetary CubeSats: Opening the Solar System to a Broad Community at Lower Cost", http://www.nasa.gov/pdf/716078main_Staehle_2011_PhI_CubeSat.pdf.

[46] S.A. Kleinfelder, E. Chiem, T. Prakash, "The SST Fully-Synchronous Multi-GHz Analog Waveform Recorder with Nyquist-Rate Bandwidth and Flexible Trigger Capabilities," Proceedings of the 2014 IEEE Nuclear Science Symposium, Seattle, WA, November 2014.

S.A. Kleinfelder, S.W. Chiang, W. Huang, "Multi-GHz waveform sampling and digitization with real-time pattern-matching trigger generation," IEEE Transactions on Nuclear Science, Vol. 60, No. 5, pp. 3785-3792, October 2013.
W. Huang, S.W. Chiang, S. Kleinfelder, "Waveform Digitization with Programmable Windowed Real-Time Trigger Capability," Proceedings of the 2009 IEEE Nuclear Science Symposium, Orlando, FL, October 2009.
S.A. Kleinfelder et al., "Design and performance of the autonomous data acquisition system for the ARIANNA high energy neutrino experiment," IEEE Transactions on Nuclear Science, Vol. 60, Issue 2, pp 612-618, April 2013.
S.A. Kleinfelder et al., "The Autonomous, Low-Power Data Acquisition System for the ARIANNA Antarctic Neutrino Detector Array," Proceedings of the 2012 IEEE Nuclear Science Symposium, Anaheim, CA, October 2012.